Graphite Electrode Characterization on the ZaP-HD Sheared-Flow-Stabilized Z-Pinch Device

Amierul Aqil bin Khairi

A thesis
submitted in partial fulfillment of the
requirements for the degree of

Master of Science in Aeronautics and Astronautics

University of Washington

2021

Reading Committee:

Uri Shumlak, Chair

Eric Meier

Program Authorized to Offer Degree:
Aeronautics and Astronautics

University of Washington

Abstract

Graphite Electrode Characterization on the ZaP-HD Sheared-Flow-Stabilized Z-Pinch Device

Amierul Aqil bin Khairi

Chair of the Supervisory Committee:
Dr. Uri Shumlak
Aeronautics and Astronautics

Applying sheared velocity flow to the Z pinch successfully mitigates MHD instabilities, enabling the concept to scale to high energy densities on the ZaP-HD device. This provides a unique platform for studying the plasma material interactions (PMI) of the coaxial configuration in a high temperature environment for a prolonged duration. The inner electrode is exposed to the plasma while forming a part of the discharge current path, resulting in significant erosion of the tungsten-sprayed copper nose cone and contamination of the plasma. A graphite nose cone was installed to investigate its material behavior and effect on pinch performance. Plasma self-emission spectroscopy and magnetic field probes were used to identify impurities, measure ion temperature, and determine stability of the pinch. The resulting pinch produced ion temperatures up to 100 eV, pinch currents of 100 kA and quiescent periods up to 57 μs. These results are comparable to the lower end of the results with copper. An initial scan of the operational parameter space included the power supply charge voltage, compression bank delay time, spectroscopy location, and spectroscopy trigger time. Considerable variability of pinch behavior between pulses was observed. A design for a removable nose cone component is presented for alternative electrode material experiments, along with extensive ex-situ surface topography measurements of targets embedded in the nose cone.

TABLE OF CONTENTS

LIST OF FIGURES

LIST OF TABLES

ACKNOWLEDGMENTS

This work would not have been possible without the guidance of my adviser, Professor Uri Shumlak. He has supported my work since my time as an undergraduate, and I am grateful for the opportunity to continue this research for my doctoral degree. I thank him for his understanding and patience throughout my time under his mentorship.

I would also like to thank Professor Brian Nelson for the countless fixes to the data server and seemingly inexhaustible trove of humorous references. I am grateful to Dr. Tobin Weber, Dr. Anton Stepanov, Dr. Yue Zhang, and Dr. Raymond Golingo for help in the day-to-day training, operation, and maintenance of the lab, and for helping me to think like a scientist. I also thank Dr. Eric Meier for his insight as I begin this study into plasma-material interactions. I am grateful to Eliot George for teaching me the techniques required to machine the graphite nose cone.

I have had the privilege of working alongside Dr. Eleanor Forbes and Dr. Elliot Claveau, who provided many moments of learning and laughter. I enjoyed the many thoughtful conversations we had in that basement office, relevant and otherwise. Thank you for your friendship and guidance. I give special acknowledgment to Aria Johansen, Tim Lloyd, Bennett Diamond, and Hannah Meek for all the support they provided on the ZaP-HD experiment.

I would like to thank the JPA and MARA agencies of the Malaysian government for supporting my studies in the United States.

Thank you to Diane Streicher and the Streicher family, whose kindness and generosity I will always remember.

Chapter 1

INTRODUCTION

Although a century has passed since it was first proposed that nuclear fusion powers the stars, the combined efforts of the global scientific community have yet to fully control this powerful energy source. As rampant energy consumption and carbon emissions continue to intensify climate change, more attention is turning to fusion as a viable component of the world's energy mix. The arrival of nuclear fusion reactors will undoubtedly mark a new era in human history, realizing the elusive dream of near-limitless clean energy.

Until then, formidable scientific and engineering challenges must be overcome. Fusion power calls for heating enough fuel mass to extraordinary temperatures for a sufficient duration. A number of configurations have been devised to fulfill these requirements, with most heating the fuel to extremely high temperatures to compensate for low density operation. Of the numerous configurations studied today, the Z pinch emerged as one of the earliest. While its simple geometry, lack of external magnets, and favorable plasma confinement are highly favorable, the Z pinch is plagued by instabilities that quickly dissipate the energy needed for fusion. However, it remains a promising design. Following successful demonstration of sheared-flow stabilization at the University of Washington, efforts to scale this concept to reactor conditions have been revitalized. The ZaP, ZaP-HD, and FuZE experiments have shown significant increases in plasma parameters based on this method, with work already underway on a device to reach energy breakeven. This increase in plasma parameters was achieved by increasing the pinch current. As the concept scales to higher plasma energy, the nature of particle and energy transfer to and from the electrode becomes increasingly important as this component provides the pinch current. Impurities from material erosion contaminate the plasma and contribute to radiation losses while damaging the electrode sur-

face. The nature of electrode interaction with a high temperature and current plasma has not been adequately studied [31]. The work presented in this thesis marks the beginning of an extended study into plasma-material interactions on the ZaP-HD experiment. In particular, it details the characterization of a graphite electrode, used as a conducting element and plasma-facing surface, and its effect on pinch performance.

1.1 History of the Z Pinch

A current flowing through a filament of conducting material will be radially compressed by the resulting magnetic forces. Lightning and solar flares are examples of natural occurrences of this pinch effect. The earliest experimental observation was made in 1790, when van Marum discharged an array of 100 Leyden jars into a long wire [18]. It wasn't until 1934 that Bennett formalized the equations describing pinch formation in conducting streams [4], noting a current threshold for the pinch effect to take place as well as favorable effects of high voltage discharge and large electrode separations. Not long after, Thomson and Blackman [17] patented a design for a thermonuclear reactor based on a toroidal pinch. A current in the toroidal direction generates a poloidal field, and the Lorentz force is radially inwards, preventing plasma interaction with the vessel walls. However, severe instabilities in the pinch caused it to strike the container, thus losing its energy and preventing further fusion reactions. Nevertheless, researchers forged ahead with the ZETA experiment, stabilizing the pinch using induced fields from an external magnet, and built the largest fusion reactor of the time. Early measurements of neutrons [35] suggested that their theory was correct, but their declaration of thermonuclear neutrons was premature. Kurchatov [23] had claimed in 1957 that the temperatures in ZETA were too low to produce the neutrons being observed, and that a different process must be the source. Further skepticism from Spitzer [6] and continued experimentation revealed that neutron spallation was the source of the neutrons, a result of strong electric fields produced by kink instabilities in the plasma. This realization condemned the stabilized pinch as a feasible fusion reactor concept, and subsequent efforts worldwide soon shifted to the tokamak.

Nevertheless, the Z pinch remains relevant as a fusion platform due to its compact design and simplicity. The current through the plasma provides ohmic heating and generates the magnetic field required for compression and confinement. This negates the need for complex, expensive magnet configurations used in other fusion concepts. This facilitates the construction and maintenance of an array of reactor cores that would constitute the fusion power plant. Ultimately, the energy released would be converted by a form of steam generator to produce electrical power for the grid.

For the same reasons, the Z pinch is suitable for use in deep space propulsion. The massive amounts of chemical propellant required for such missions preclude traditional chemical propulsion systems from being viable. Current advances in electric propulsion provide a low fuel mass, high efficiency solution to space travel, but is limited by the amount of power available on-board. A lightweight Z-pinch fusion reactor could provide the power needed to scale electric propulsion systems for future missions. Furthermore, the linear geometry of a Z pinch means it is well-suited to function as a fusion thruster. This concept involves exhausting the fusion products directly out of a magnetic nozzle to provide thrust.

1.2 Z-Pinch Fusion

Nuclear fusion involves the collision of two atomic nuclei which combine to form a nucleus of greater atomic number. By mass-energy equivalence, the energy released in this reaction is related to the mass difference between the fusion products and reactants. Fusion reactions of light elements releases significant amounts of energy due to the dominance of the nuclear strong force. In contrast, combustion of fossil fuels is related to the rearrangement of electrons in the molecules involved, a process dominated by the electromagnetic force. The relative strength of these forces is such that the energy released from a nuclear reaction is a million times greater per reaction [14]. The main challenge is that to enter the range of the attractive strong force, the nuclei must have enough energy to overcome the repulsive electrostatic Coulomb force. The relevant reactions for fusion are given as follows:

$$D + D \rightarrow {}^{3}\mathrm{He} + \mathrm{n} + 3.27\ \mathrm{MeV} \tag{1.1}$$

$$D + D \rightarrow \mathrm{T} + \mathrm{p} + 4.03\ \mathrm{MeV} \tag{1.2}$$

$$D + {}^{3}\mathrm{He} \rightarrow \alpha + \mathrm{p} + 18.3\ \mathrm{MeV} \tag{1.3}$$

$$D + T \rightarrow \alpha + \mathrm{n} + 17.6\ \mathrm{MeV} \tag{1.4}$$

Equations 1.1 and 1.2 represent two possible branches of a collision between two deuterium (D) ions, each with an equal likelihood of occurring. The products are helium-3 (^{3}He) and a neutron (n), or tritium (T) and a proton (p). This D-D reaction has the benefit of a near unlimited fuel supply since deuterium is readily available from ocean water. However, it is difficult to initiate and is less energetic than the other reactions. Equation 1.3 is considerably more energetic, but ^{3}He does not occur naturally. Notably, the reaction products are both charged particles, perhaps enabling direct electricity generation if the fuel can be obtained. Neutron activation and radiation damage also pose less of an issue. Finally, the D-T reaction in Equation 1.4 is the easiest to initiate, with a high energy neutron produced. This is the reaction of choice for the global fusion program.

Despite its history, the Z pinch has persisted in various forms, finding use as an X-ray generator and notably in inertial confinement fusion devices. The Z Pulsed Power Facility at Sandia National Laboratory implodes an array of tungsten wires by the pinch effect, releasing heat in the form of X-rays [16]. Data collected from this type of high energy environment informs simulations of nuclear explosions and supports management of the nuclear stockpile of the United States. The same facility also investigates the Z pinch for use in a form of inertial confinement fusion known as MagLIF, or Magnetic Liner Inertial Fusion. Like a true ICF device, a laser is used to heat deuterium gas in a hohlraum target, but compression is achieved by an intense pulse that forms a Z pinch, magnetically imploding the fuel. Experiments at the Z facility have produced $2\text{x}10^{12}$ thermonuclear neutrons from D-D reactions at decreased implosion velocity and pressures, marking a significant improvement on purely laser driven devices [16].

1.3 Equilibrium and Stability

Development of a Z pinch based reactor has stagnated mainly due to difficulties in controlling virulent instabilities, leading the plasma to collide with the vessel walls and cool down. To understand the nature of these instabilities, the equilibrium of the configuration is considered. Assuming the case of one dimensional MHD for a pure Z pinch, the radial pressure balance is described by the following equation:

$$\frac{d}{dr}(p + \frac{B_\theta^2}{2\mu_0}) + \frac{B_\theta^2}{\mu_0 r} = 0 \tag{1.5}$$

The terms in the derivative are the plasma pressure and the magnetic pressure. The third term, the magnetic tension, arises from the magnetic field curvature and provides the radial force balance. Instabilities are a result of the runaway growth of perturbations from this equilibrium. While there are several instabilities relevant to the Z pinch, this paper is concerned with the m = 0 sausage mode and the m = 1 kink mode.

The m = 0 sausage mode begins as a perturbation in the plasma column resulting in a decrease of the radius at some axial location. There is a corresponding increase in radius just upstream and downstream, shown in the left hand side of Figure 1.1. The total current through the plasma cross section is constant, therefore the azimuthal magnetic field at the reduced radius is larger than locations with larger radius. The magnetic field scaling with radius is $B_\theta \sim 1/r$. The radial force balance is changed such that there is now a net force inward at this location. Conversely, an expansion of the column at the location of larger radius occurs due to an imbalance of the forces that is directed outward. The perturbation continues to grow, resulting in instability and the eventual loss of the pinch when the constriction halts the current flow. The m = 1 kink instability results from an initial perturbation that bends the plasma column, shown in the right hand side of Figure 1.1. In the region of stronger curvature, the field strength increases due to the greater field line density.

The corresponding weaker curvature causes a decrease in field strength. The increased tension inside the curve and the decreased tension outside the curve form a force distribution that causes the perturbation to grow. The pressure term in Equation 1.5 is defined as:

$$p = n_i k_B T_i + n_e k_B T_e \tag{1.6}$$

Assuming a quasi-neutral plasma, then the electron and ion densities are related by $n_e = Z n_i$, where Z is the ionization state. T_i and T_e are the ion temperature and electron temperature respectively, and k_B is the Boltzmann constant. The integration of Equation 1.5 is carried out over the plasma volume, and incorporates the following definitions of the linear ion number density N_i and average temperature $\langle T \rangle$:

$$N_i = \int_0^a \int_0^{2\pi} n_i r d\theta dr \tag{1.7}$$

$$\langle T \rangle = \frac{1}{\pi a^2} \int_0^a \int_0^{2\pi} T r d\theta dr \tag{1.8}$$

Here, a is the pinch radius. It is assumed that $T = T_i = T_e$. The result is the Bennett relation [4]:

$$(1 + Z) N_i k_B \langle T \rangle = \frac{\mu_0 I^2}{8\pi} \tag{1.9}$$

The density heavily depends on the axial plasma current I. Therefore, the process of scaling the shear flow stabilized Z pinch to higher plasma parameters centers is centered on increasing the plasma current. Further scaling relations can be derived relating an increased current to increases in magnetic field, temperature, and decrease in pinch radius. Note that

the validity of these relations depends on the approximation of adiabatic compression, where the time scale of plasma compression is sufficiently fast that there is no time for heat to enter the system.

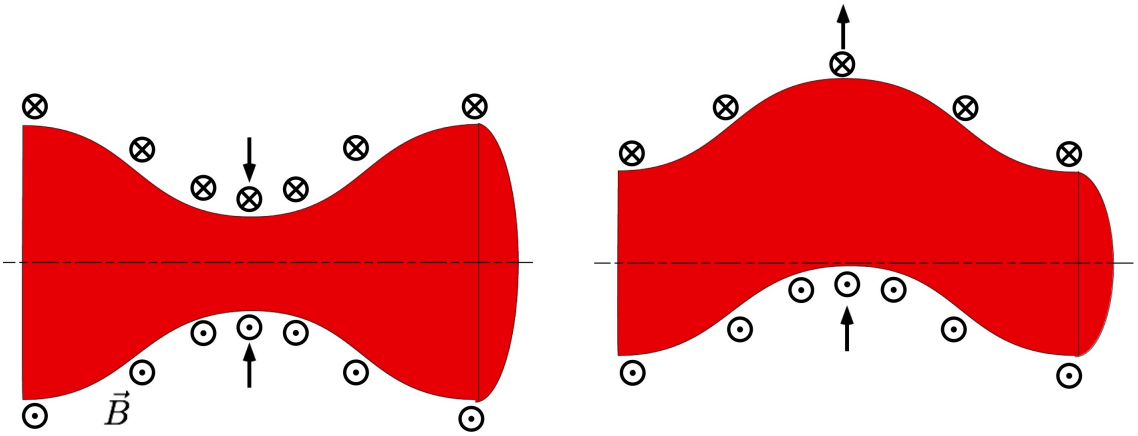

Figure 1.1: The left hand side image shows the m = 0 sausage mode instability. An increase in magnetic field at the location of decreased radius causes further constriction. The right hand side shows the m = 1 kink mode. A slight bend in the plasma causes a region of increased magnetic field inside the curve and a net force that increases the curvature. The instability grows until the pinch is disrupted.

Several methods of stabilizing the Z pinch have been investigated. Shafranov [30] obtained stability conditions by applying a longitudinal magnetic field. However, these axial field lines are necessarily open and result in losses to the electrodes in a pinch configuration. Additional cost and complexity are introduced by the external field coils, which negate a primary advantage of the Z pinch. Dynamic "fast" Z pinches rely on achieving formation and compression before the instability growth time. Typically, these take the form of solid annular liners and wire arrays coupled to extensive pulsed power systems [18]. The drawback here is that any radial equilibrium that is reached is highly transient. To take advantage of the strong scaling of fusion performance with current, a longer-lived radial equilibrium is necessary. The m = 1 instability can be mitigated by placing a conducting wall within 20% of the pinch radius [32]. However, the extreme temperatures that such a wall would be exposed to make this concept unfeasible in practice. The m = 0 sausage mode can be stabilized by specifying the radial pressure profile [20] , but not the m = 1 kink mode.

1.4 Sheared-Flow Stabilization

As discussed previously, an axial field can be used for the purpose of stabilization, but comes at a price. An additional caveat is that an axial field limits the axial current, a highly undesirable outcome given the role of the current in heating and compression. However, a numerical study by Shumlak [32] demonstrated that the m = 1 mode can be stabilized by the application of enough axially sheared flow. For a wall radius at least 4 times as large as the pinch radius, the radial shear must be above or equal to the following threshold:

$$\frac{dv_z}{dr} \geq 0.1 k V_A \tag{1.10}$$

Here, $\frac{dv_z}{dr}$ is the radial velocity gradient, k is the wave number, and V_A is the Alfvén speed defined by the maximum field and density:

$$V_A = \frac{B_0}{\sqrt{\mu_0 \rho_0}} \tag{1.11}$$

Physically, given that the m = 1 mode can propagate at the average plasma velocity, the existence of a non-uniform plasma velocity interrupts the growth of the perturbations. The velocity differential across the pinch counteracts the m = 1 mode and prevents the magnetic field from continually increasing.

1.5 The Flow Z-Pinch Experiments

A series of experiments at the University of Washington applied the sheared-flow stabilization concept. The ZaP, ZaP-HD, and FuZE flow Z pinches have achieved orders of magnitude increases in plasma parameters while maintaining a stable pinch for thousands of instability growth times [12]. The shear flow was achieved by puffing neutral gas into a coaxial electrode configuration. The design coupled two main sections: an upstream section for ionization and acceleration and a downstream section for pinch assembly. The original ZaP experiment produced pinch currents up to 100 kA and a pinch radius on the order of a centimeter [12]. The ZaP-HD (High Density) experiment was designed with two separate power supplies, one each for the acceleration and assembly regions, thus enabling greater control over experimental parameters. To allow for this system, a triple coaxial electrode configuration was built. Subsequently, the FuZE device was the first to achieve fusion-relevant plasma parameters, and has made observations of thermonuclear neutrons [36]. Table 1.1 lists a selection of plasma parameters for the three experiments. While ZaP-HD was not designed to produce fusion reactions, its high density and temperature environment are still highly useful for additional reactor-relevant studies.

Parameter	ZaP	ZaP-HD	FuZE
Plasma current (kA)	100-200	300	300-600
Pinch current (kA)	50-100	150	150-300
Pinch radius (cm)	0.5-1	0.2-0.5	0.1-0.3
Electron density (cm^{-3})	10^{16}	10^{17}	$> 10^{17}$
Temperature (eV)	100	1000	>1000

Table 1.1: Comparison of pinch performance for the Flow Z-Pinch experiments at the University of Washington.

Chapter 2

THE ZAP-HD EXPERIMENT

The ZaP-HD device was designed to demonstrate that high energy density plasmas could be achieved using sheared flow stabilization. It is well studied [33] with an extensive diagnostic suite. Similarly to the original ZaP experiment, ZaP-HD formed a flow Z pinch by coupling a plasma acceleration region to a pinch assembly region. In ZaP, both of these regions are defined by sections of two coaxial electrodes. ZaP-HD modified this design with an additional third coaxial electrode in order to increase control over the plasma current via two separate capacitor banks, shown in Figure 2.1. Plasma acceleration is initiated by discharging the bank between the inner and the middle electrode. Plasma compression is controlled by discharging the bank between the inner and outer electrodes. Eight Parker fast puff valves are positioned azimuthally outside of the electrodes, while a single valve is mounted axially inside the inner electrode. A separate circuit individually controls the inner valve and two sets of four outer valves, enabling control of injection timing. The acceleration region is 1 meter long, spanning the distance between the azimuthal gas injection plane and the tip of the tapered nose cone. The assembly region extends a further 50 centimeters to the end wall of the outer electrode. Axial locations are denoted in centimeters, with the nose cone tip as a reference point. Locations in the acceleration region are designated "N5", "N10" and so on, while "P0", "P15", and so on denote assembly region locations. Three fused silica rectangular windows allow viewing of the pinch.

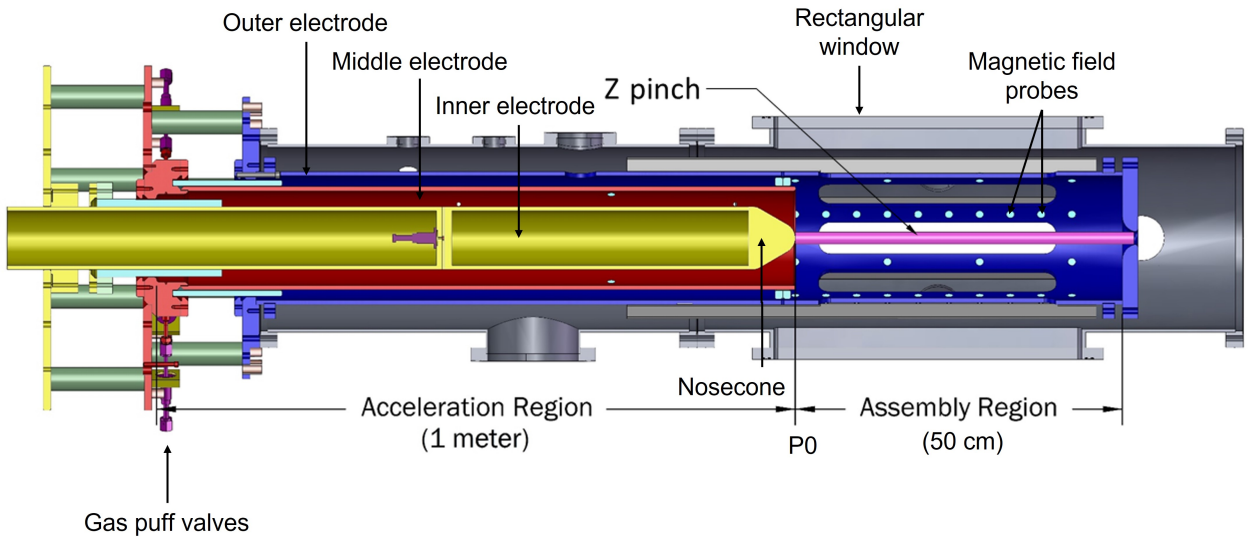

Figure 2.1: A cross-sectional view of the ZaP-HD device. The vacuum chamber (gray) encloses the three coaxial electrodes: the outer electrode (blue), middle electrode (red), and inner electrode (yellow). Neutral gas is injected by eight azimuthal gas puff valves and one axially aligned valve (purple) into the annular region between the inner and middle electrode. This one-meter length defines the acceleration region, which terminates at the tapered nose cone. The Z pinch is formed in the 50 cm long assembly region, which is equipped with multiple arrays of magnetic field probes for pinch characterization.

2.1 Pinch Formation

The following steps are described in Figure 2.2a. The process of forming a pinch begins with injection of neutral gas (blue) into the annular region between the middle and inner electrodes. Once the neutral gas, typically hydrogen, has been injected and expands, a Ross relay circuit discharges one capacitor bank through an ignitron switch. This discharge initiates breakdown of the neutral gas into plasma (red), allowing current flow (green) between the inner and middle electrodes. The Lorentz force then accelerates the plasma downstream until the end of the inner electrode, forming a snowplow front.

The remaining steps are illustrated by Figure 2.2b. The second power supply is discharged between the inner and outer electrodes, driving additional plasma current. The power supply used for compression consists of two capacitor banks, each with its own ignitron switch. The field from this current compresses the plasma into a pinch structure with axial current and azimuthal field. Residual gas upstream is ionized and accelerated in a similar manner, supplying additional plasma into the pinch. The plasma temperature increases through Ohmic heating by the driven current. The pinch is sustained until the residual gas in the accelerator depletes, the capacitor bank current ceases, or by succumbing to instabilities.

2.2 Diagnostics

An extensive selection of diagnostic methods have been developed to characterize the plasma, including magnetic field probes, Rogowski coils, spectroscopy, interferometry, and high-speed imaging. Data acquisition modules are armed prior to a plasma pulse, and record the data to a central server immediately following the end of a pulse. Specific trigger times for particular diagnostics can be set according to the needs of the operator. This study used the magnetic field probes, Rogowski coils, ion Doppler spectroscopy, and high-speed imaging diagnostic systems.

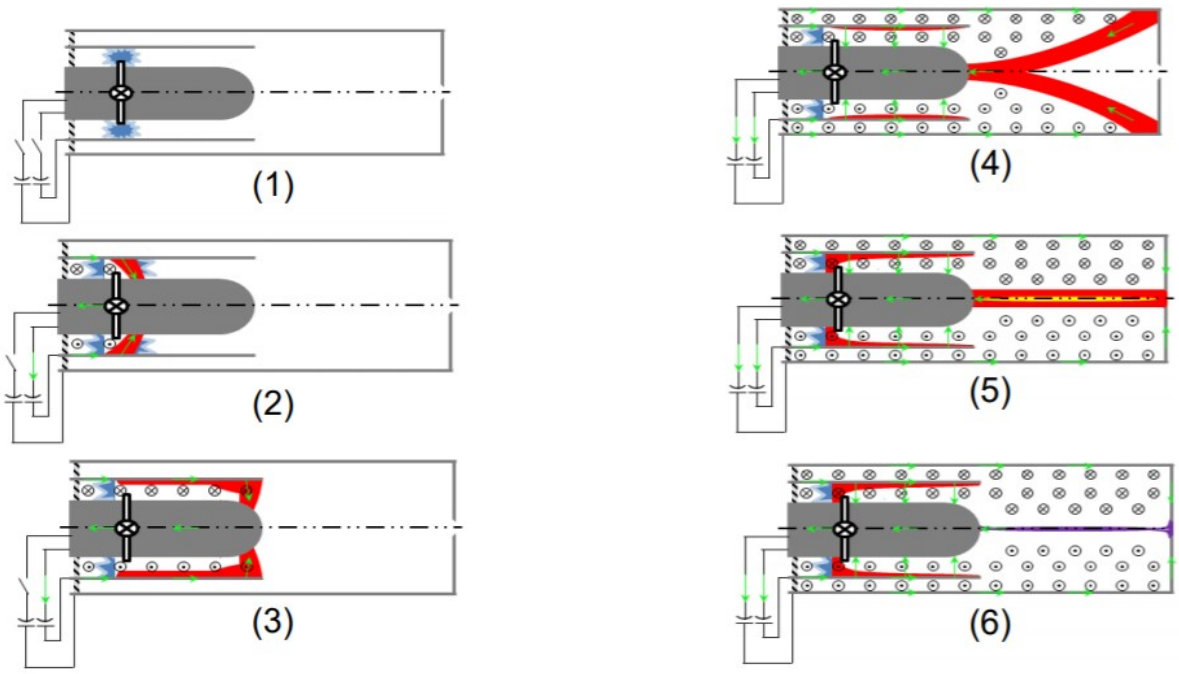

(a) (b)

Figure 2.2: Formation of the sheared-flow stabilized Z pinch in a coaxial electrode configuration.

2.2.1 Magnetic Field Probes

The azimuthal field is measured by exploiting Faraday's Law, which describes an induced voltage from a change in magnetic flux.

$$\int \frac{d\vec{B}}{dt} \cdot d\vec{S} = -\oint \vec{E} \cdot d\vec{l} = -V_i \tag{2.1}$$

Magnetic probes consist of a coil of conducting wire that defines a cross-sectional area A. A time-changing magnetic field $\frac{d\vec{B}}{dt}$ through the coil area induces a voltage V_i across the ends of the leads. This voltage is related to the time derivative of the field and the number of turns in the coil N as in Equation 2.2:

$$V_i = -N \int \frac{d\vec{B}}{dt} \cdot d\vec{S} \tag{2.2}$$

Performing a time integral and rearranging for the average magnetic field results in the following relation:

$$B_{avg}(t) = -\frac{1}{NA} \int_0^t V_i dt \tag{2.3}$$

In practice, the average field is obtained by integrating the measured voltage signal and multiplying by a calibration factor consisting of the number of turns N and the coil area A. The probes on ZaP-HD consist of turns of 32 gauge magnet wire around an insulating Kel-F core. This is bonded with Torr Seal to a boron nitride shield, which faces the plasma. There are 15 probes embedded into the middle electrode, corresponding to the acceleration region, and 56 probes in the outer electrode for the assembly region. Figure 2.3 shows the placement of probes in the assembly region. An azimuthal array of four probes is located

every five centimeters, and an array of eight every 15 centimeters. This allows for an axial and azimuthal resolution of the magnetic field topography.

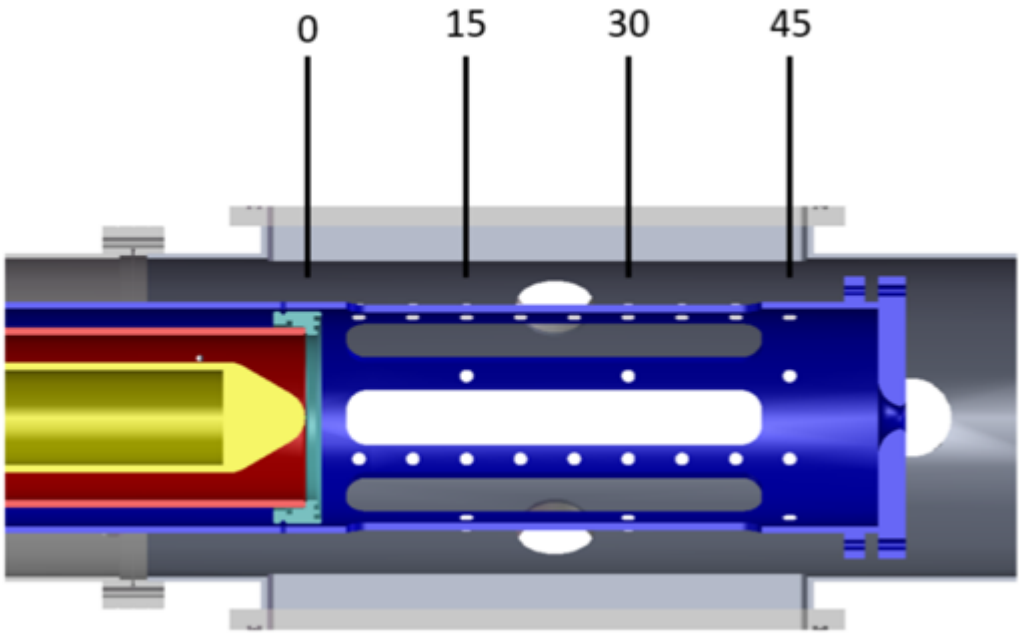

Figure 2.3: Locations of the magnetic field probes in the assembly region. Probe arrays are spaced 5 centimeters apart. There are only four arrays with eight azimuthal probes, at P0, P15, P30 and P45.

2.2.2 Ion Doppler Spectroscopy

Plasma emits light over a broad range of wavelengths, and this emission strongly depends on the plasma properties. Analysis of the plasma self-emission provides a measurement of these properties without perturbing the plasma. Radiation from the plasma originates from energetic interactions of electrons within the plasma. Broadband radiation is observed when a free electron is deflected from its path by the Coulomb force of an ion. Because the electron has been decelerated, its kinetic energy has decreased. The lost energy is emitted as a photon to satisfy conservation of energy. This is known as bremsstrahlung radiation and produces a continuous spectrum. Conversely, bound electrons that are still associated with their nuclei can emit radiation through successive excitation and decay between energy levels. Collisions with free electrons provide the energy for these transitions. The quantized energy levels result in highly distinct photon wavelengths and appear as emission lines in a spectrum.

The working gas in ZaP-HD is hydrogen, therefore there are no bound electrons remaining once the atom is ionized. Therefore, impurity elements such as carbon and oxygen are seeded into the device to obtain spectroscopic data. Because of the increasing ionization energies required to remove successive electrons, the presence of multiple ionization states of the impurities is a qualitative measure of the plasma temperature. Quantitatively, the temperature is determined by examining the Doppler broadening. This is the broadening of spectral lines due to the distribution of particle velocities in the plasma. The wavelength of observed radiation from each of these particles is Doppler shifted, effectively widening the recorded line spectra. Analysis of Doppler broadening is presented by Hutchinson [19], using shifted frequency f, actual frequency f_o, and particle velocity v. The frequency shift Δf is defined as:

$$\Delta f = f - f_o = \frac{f_o v}{c} \tag{2.4}$$

Here, c is the speed of light. The velocity is rewritten in terms of the frequencies:

$$v = c(\frac{f}{f_o} - 1) \tag{2.5}$$

Assuming a Maxwellian distribution of velocities leads to a Gaussian profile F_G:

$$F_G(f) = F_G(f_o)exp[\frac{-(f - f_o)^2 c^2 m_i^2}{2k_B^2 T_i^2 f_o^2}] \tag{2.6}$$

Here, m_i is the ion mass and T_i is the ion temperature. Typical analysis of Gaussian profiles uses the full width at half maximum (FWHM):

$$\Delta f_{FWHM} = f_o\sqrt{\frac{8k_B T_i \ln 2}{m_i c^2}} \tag{2.7}$$

In practice, the recorded spectra are plotted in terms of the wavelength. The equivalent equation for FWHM then becomes:

$$\Delta \lambda_{FWHM} = \lambda_o\sqrt{\frac{8k_B T_i \ln 2}{m_i c^2}} \tag{2.8}$$

Ion Doppler spectroscopy on ZaP-HD uses two telecentric telescopes to collect light. The telescopes view the plasma through the top rectangular window. The radial telescope is perpendicular to the pinch axis, and therefore does not view any bulk plasma Doppler shift. The oblique telescope is 45 degrees from the pinch axis. Since a component of the plasma flow is normal to the telescope lens, the oblique telescope enables calculation of the bulk flow velocity. Because of random thermal particle motion in all directions, both telescopes can record Doppler broadening. Currently, only the oblique telescope is installed on the device, shown in Figure 2.6. The telescopes focus the light into a bundle of twenty fiber optic chords. Figure 2.4 shows the configuration of the "wide" fiber optic bundle.

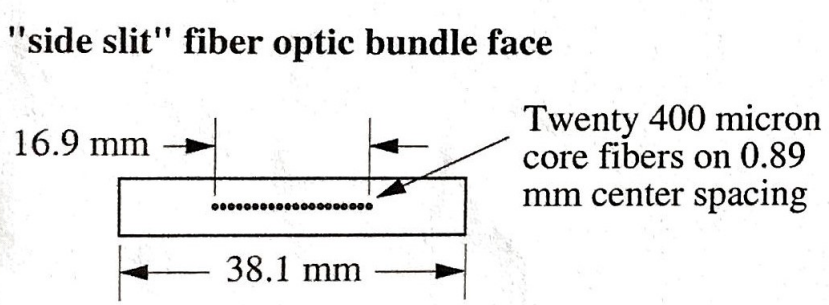

Figure 2.4: The wide fiber optic cable bundle mounted on the oblique telescope. Light is incident on twenty 400 micron core fibers with 0.89 mm center spacing and 16.9 mm total width. "Side slit" refers to one of the two input mirros on the Acton spectrometer, the other position being the "front slit" [10].

The optical fibers feed back into an Acton 500i spectrometer, which uses a blazed diffraction grating to sort the light by wavelength. Incident light from the fibers is dispersed by the grooves in the grating. Light is diffracted off the grating and an interference pattern is recorded with the wavelength of interest appearing at a maximum. Rotation of the grating allows selection of this wavelength. The Acton is coupled to a Roper Scientific Pi-MAX Intensified Charge-Coupled Device (ICCD) detector, which records a single spectrum on each trigger. The ICCD gain, gate duration, and trigger time are adjusted to image periods of interest during the pinch, where a balance is struck between strong, uniform illumination across all 20 chords and avoiding saturation. An example of a recorded spectrum for the carbon-III ion is shown in Figure 2.5. The ICCD image is 512 by 512 pixels. The chords appear as a vertical line at the target wavelength, with intensity mapped as a color gradient. For this spectrum, intensity is high at the center of the image, corresponding to greater captured emission at the center of the plasma. At the top of the image the intensity drops significantly and the wavelengths appear to be slightly shifted away from the nominal value. Counting up from the bottom of the image, this is seen for chords 16-20.

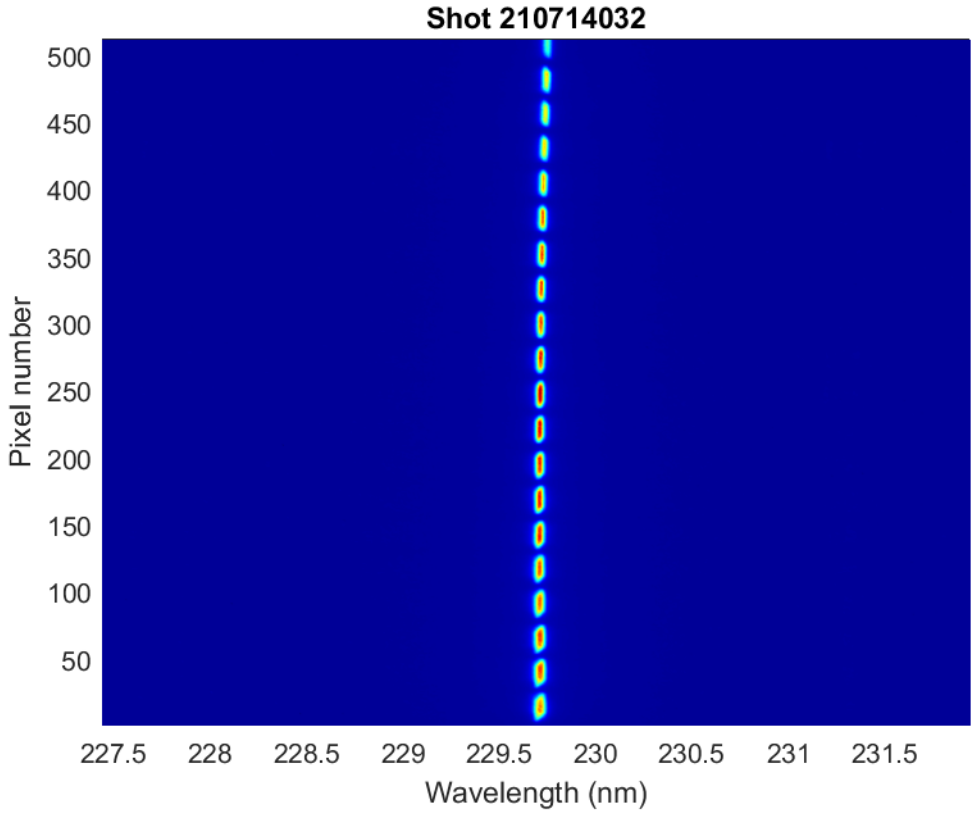

Figure 2.5: An example of the spectral output from the ICCD detector for the carbon-III ion. The image is 512 x 512 pixels large. All 20 chords from the wide fiber bundle are clearly visible and centered on 229.7 nm. Each chord is colored according to the light intensity recorded by the ICCD. Blue is near zero intensity, while red indicates high intensity up to the saturation limit of $I = 65000$.

A typical impurity line observed on ZaP-HD is from the carbon-III (C-III) ion at 229.687 nm. The numeral indicates the electron responsible for emission beginning from the outermost electron. For the C-III ion the electron undergoing excitation and decay is the third outermost electron, as the first two electrons have already been removed. This is a strong line that consistently appears throughout a pulse duration, making it useful for measuring velocities. For higher energy pulses a further two electrons are stripped, and the C-V triplet lines become visible at 227.089, 227.727 and 227.792 nm. Wavelength references are used from the NIST Atomic Spectra Database [22].

2.2.3 High-Speed Imaging

A Kirana 05M Ultra-Fast Framing camera is used to obtain qualitative information during each plasma pulse. The Kirana can take 180 frames at a resolution of 924x768 pixels and has a dynamic range of 10 bits. With speeds up to 5 million frames per second and shuttering down to 100 ns, it is well suited to capturing phenomena on the microsecond scale, rendering detailed images of pinch assembly, collimation, and growth of instabilities. Its compact design allows for flexibility in placement to fully utilize the windows around the assembly region. Images are typically recorded in the visible spectrum, although a phosphor intensifier can be installed to view ultraviolet emission.

The Kirana is mounted on a tripod or placed on one of the optical tables located on either side of the ZaP-HD device. A periscope structure consisting of a set of mirrors in a 3D-printed bracket enables imaging from the top window, shown in Figure 2.6. A set of images from a Kirana video depicting pinch formation and destabilization is shown in Figure 2.7. The video was taken at 4 million frames per second and 250 ns exposure per frame. The Kirana was angled slightly upstream to view the nose cone, which is silhouetted against the bright plasma to the right of the images. These images only show the view from the side window, with the downstream direction to the left. The first image, Figure 2.7a, shows the plasma without any collimated structure. The isolated bright region in the left hand side is a reflection off of the far-side window. Figure 2.7b shows a well-defined, centered pinch.

There is a large area of current attachment on the nose cone. In Figure 2.7c there is still a structured pinch, although a kink instability is visible. By Figure 2.7d, the plasma is highly unstable and the pinch is disrupted.

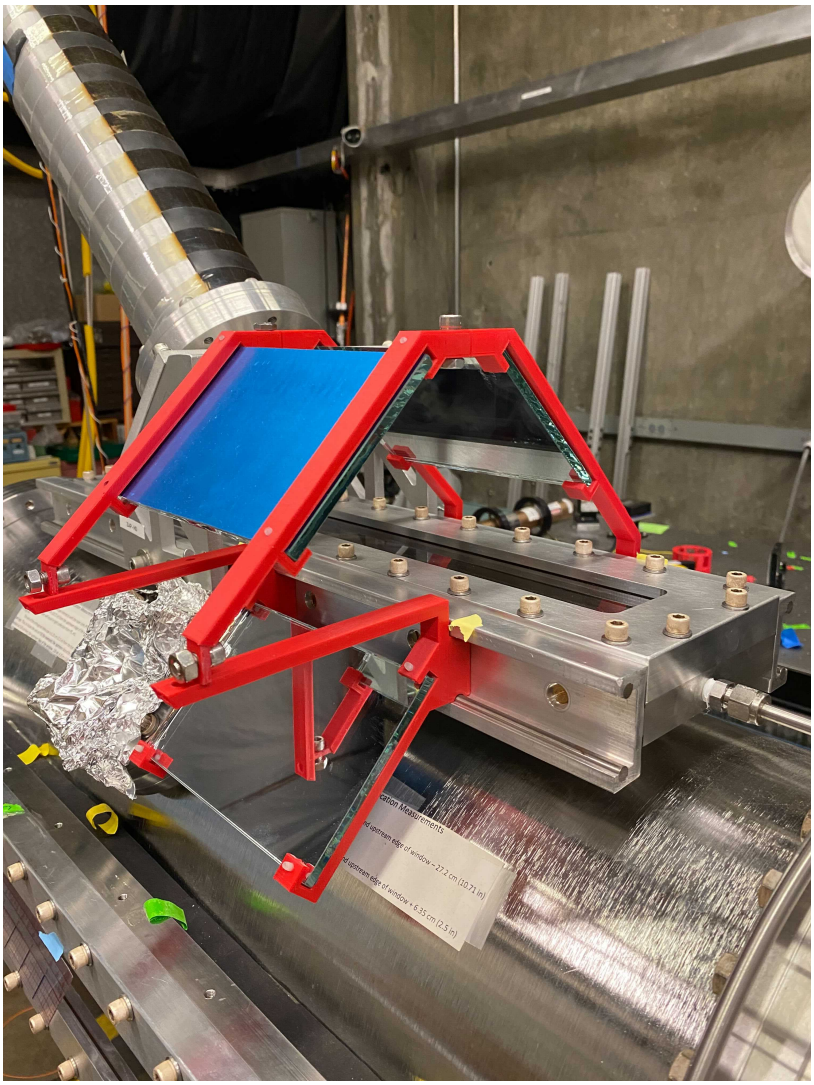

Figure 2.6: A 3D-printed bracket and three mirrors form a periscope allowing the Kirana camera to view the light from the top window. The side window is in the bottom-left of the image. The Kirana is on a table located to the left of this view. The oblique telescope is mounted on the top window in the background.

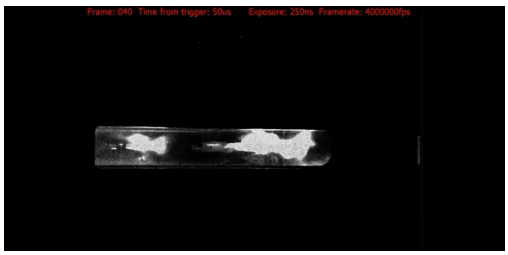

(a) 50 μs

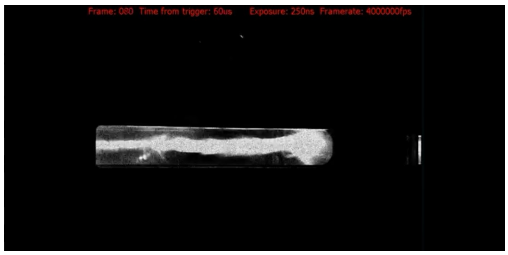

(b) 55 μs

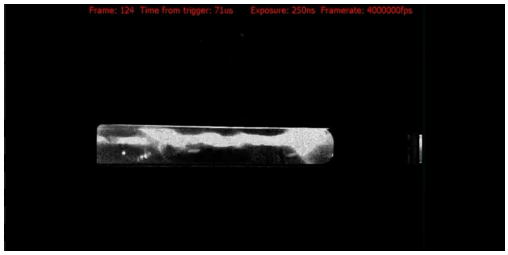

(c) 71 μs

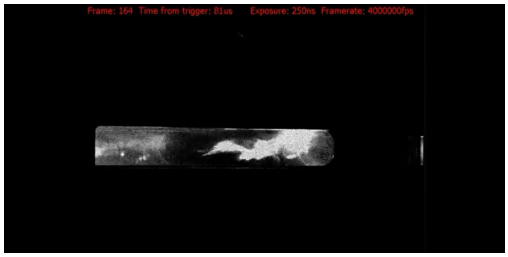

(d) 81 μs

Figure 2.7: Individual frames from a high-speed recording using the Kirana camera at 4 million frames per second and 250 ns exposure per frame. View is only from the side window with the downstream direction to the left. The images show the progression of the pinch structure: a) no pinch structure, b) well-defined pinch, c) onset of instabilities, d) loss of the pinch column. Images are from pulse 210203029.

2.3 Pinch Characterization

The various diagnostics are used in concert to build a picture of the pinch behavior in time and space. Data collection occurs continuously before and after the initial experimental trigger at $t = 0$. Events such as plasma disruptions due to instabilities will appear on multiple signals. For example, an instability will cause a high amplitude peak in the magnetic field data, with a corresponding peak in the plasma current and voltage measurements. Conversely, a period of stability involves peak pinch current and low magnetic mode values. Correlation of signals is essential in determining whether an event was recorded faithfully or if a fault in the data acquisition or processing is the cause. In general, a stabilized pinch is marked by low fluctuation of the axial magnetic field, high density and ion temperature, and a measurable radial velocity shear. This study is limited to the measurement of magnetic field, currents, and ion temperature.

2.3.1 Plasma Parameters

The ion temperature is extracted from Doppler broadening of the plasma self-emission. Each of the 20 chords shown in Figure 2.5 has a distribution of intensity about the center wavelength of C-III. In Figure 2.8, the corresponding Gaussian profiles are shown in red and fitted to each chord's distribution. The FWHM is calculated for each chord, and the ion temperature calculated using Equation 2.2.2. As seen previously, the higher numbered chords have distributions that have shifted away from the nominal C-III wavelength. The results are plotted in Figure 2.9. The bars correspond to a 95% confidence interval.

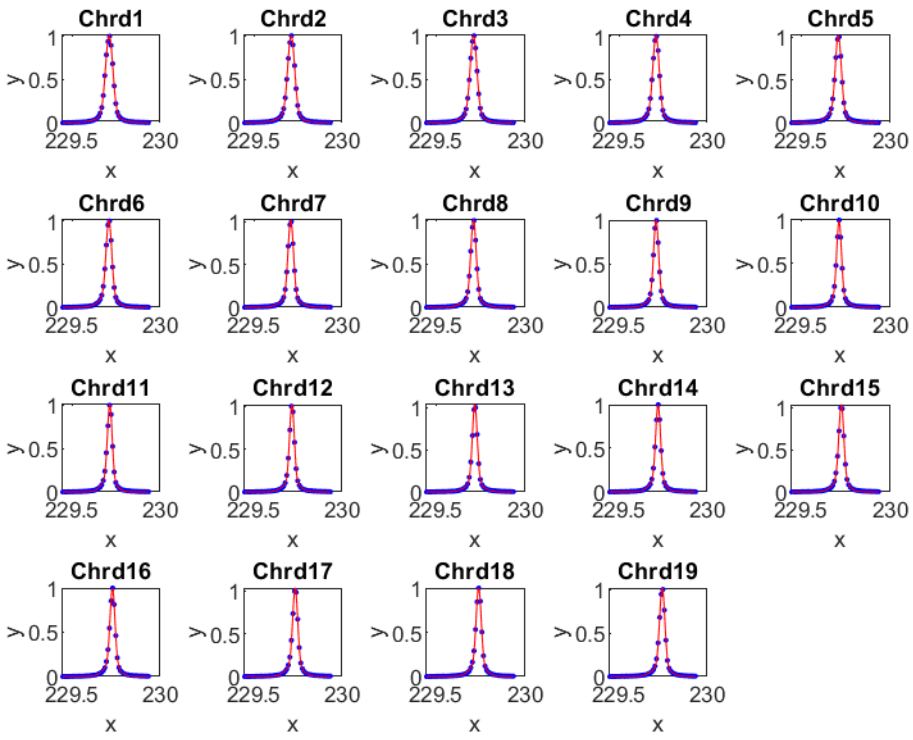

Figure 2.8: Fitted Gaussian profiles are shown in red for each of the 20 chords in the wide fiber bundle and the oblique telescope. Blue dots represent the recorded light intensity around the center wavelength for C-III. The FWHM of the profiles is used to calculate the ion temperature. Data are from shot 210714032.

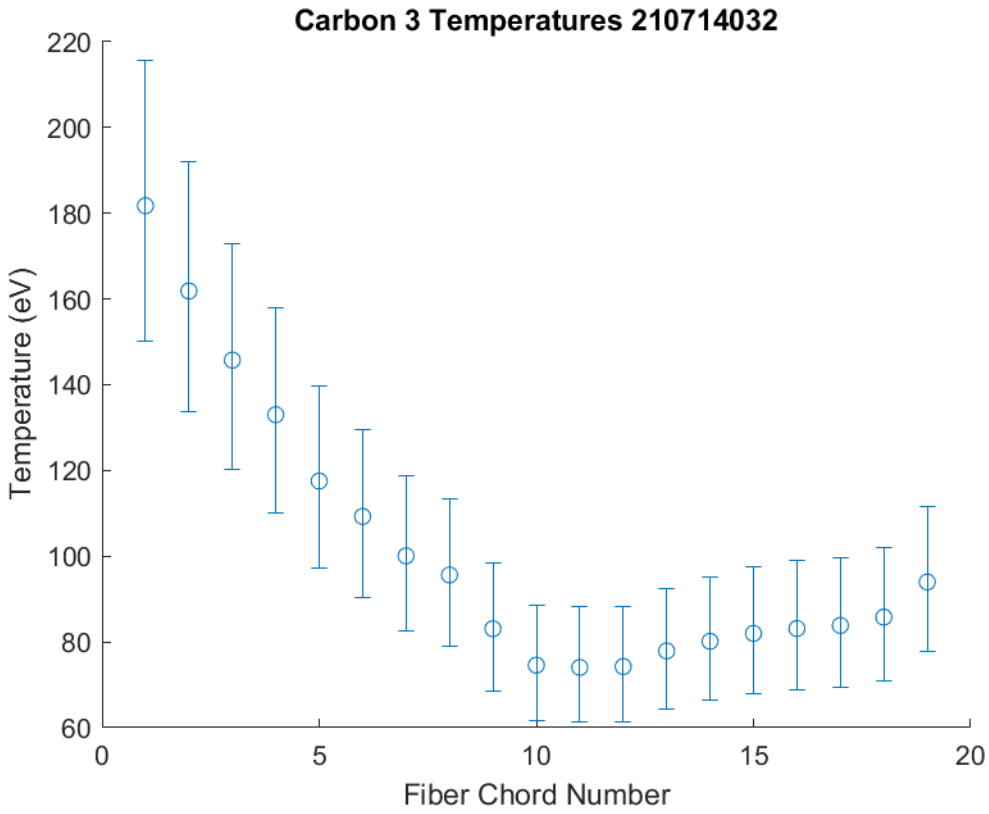

Figure 2.9: A plot of ion temperatures calculated for each chord of the wide fiber bundle viewing light through the oblique telescope. Temperatures appear to be lowest at the center of the bundle. There is a significant decrease in temperature from the edge of the bundle. The bars correspond to a 95% confidence interval.

2.3.2 Stability and Quiescence

Pinch stability is determined using data from the magnetic field probes. The voltage measured across the leads of the probes is integrated with DAFI analog integrators. The signal then directly represents the magnitude of the field being measured, and is then digitized. Calculation of the m = 0 and m = 1 modes begins by assuming the signal is of the form:

$$B_\theta(\theta_i) = \sum_{j=0,m} a_j cos(j\theta_i) + \sum_{j=1,m} b_j sin(j\theta_i) \tag{2.9}$$

B_θ is the azimuthal field, θ_i is the azimuthal probe location in radians, and a_j and b_j are unknown Fourier coefficients. The index j refers to the mode number. The azimuthal mode amplitudes are determined by solving for the coefficients. The measured field, coefficients, and trigonometric terms are placed into arrays **B**, **C**, and **A** respectively. Taking the pseudo-inverse of **A** returns the matrix of coefficients:

$$\mathbf{C} = (\mathbf{A}^T\mathbf{A})^{-1}\mathbf{A}^T\mathbf{B} \tag{2.10}$$

Further detail into this process is described by Golingo in his dissertation [15]. Using the coefficients, the mode amplitude and phase are calculated with the following equations:

$$m_j = \sqrt{a_j^2 + b_j^2} \tag{2.11}$$

$$\phi_j = tan^{-1}(\frac{b_j}{a_j}) \tag{2.12}$$

The eight-probe azimuthal arrays on ZaP-HD are capable of resolving up to 3 modes, since any mode m_j requires $2m_j + 1$ probes. However, only the first two modes, m = 0 and m = 1 are needed to define pinch stability. The m = 0, or m_0, mode represents the mean

amplitude of the magnetic field, while m_1 describes the radial displacement of the current centroid from the center of the probe array. The value of m_1 is normalized by the maximum m_0 and satisfies the following relation:

$$\frac{m_1}{m_0} = 2\frac{\Delta r}{r_{wall}} \tag{2.13}$$

Here, Δr is the pinch displacement, and r_{wall} is the radius of the vessel wall. Given an r_{wall} of 10.8 cm, a normalized m_1 value of 0.2 means that the current is displaced by 1 cm. A stable, or quiescent, pinch is then defined as having normalized m_1 be less than 0.2 for a non-zero m_0 over an extended time. The second condition is necessary to qualify quiescence for times when there is a finite current.

Figure 2.10 is an example of a typical plot showing the normalized m_1 mode data, plasma current and pinch current. The black trace represents an axial mean along the assembly region, with its standard deviation plotted in gray. The plasma current represents the total current discharge from the power supplies, while the pinch current is calculated from magnetic field data at a certain axial location in the assembly region. The sudden increase in plasma current around 25 μs is caused by the discharge of the compression bank which is delayed to allow time for plasma to enter the assembly region. Oscillations in plasma current often occur immediately after discharge and is reflected by oscillations in the m_1 data. However, when the plasma and peak currents pass through their maximum, the m_1 mode is suppressed below the threshold for quiescence, here occurring between 35 and 68 μs. As the current and neutral gas supply decrease, instabilities begin to dominate and dissipate the pinch, and the m_1 mode rises above the threshold.

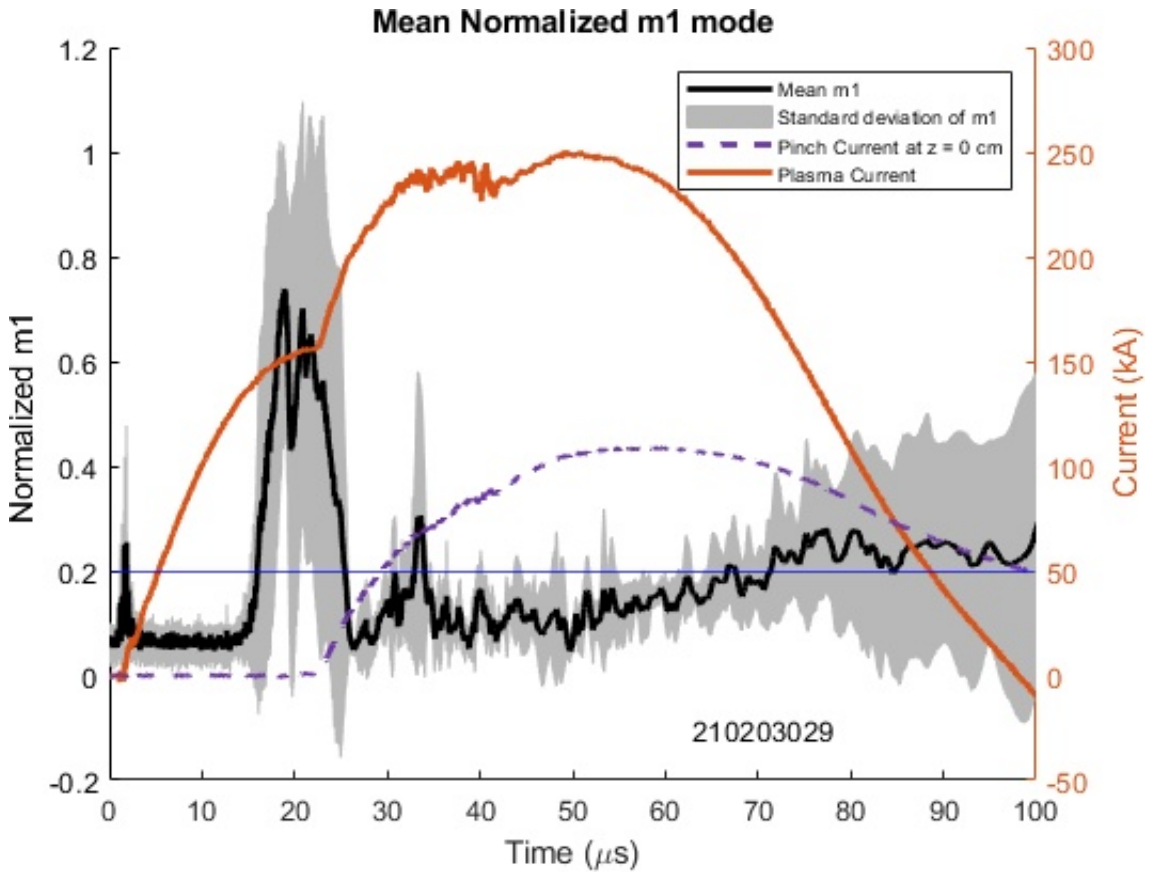

Figure 2.10: Example of magnetic mode and current data from a single pulse. The mean m_1 trace is in black with standard deviation in the gray fill. Plasma current is in orange and pinch current at z=0 is the purple dashed line. The quiescent period for this pulse begins around 35 μs and ends around 68 μs. The mode data is below the threshold during the time that the currents pass through their maximum values.

Chapter 3

PLASMA MATERIAL INTERACTIONS

Any reactor configuration designed to contain a fusion plasma must contend with extraordinary particle flux and energy. The extreme temperatures attained by the plasma surpass the physical limitations of any conceivable wall material. Therefore, plasmas are contained with magnetic fields. However, plasma facing surfaces are not entirely avoidable, and are often a useful design component. In equilibrium, the edge plasma will interact with the solid wall, and as instabilities grow the energy flux to the wall increases, eventually resulting in loss of confinement as the plasma cools. In addition, ion impacts on the solid material can be energetic enough to cause sputtering of atoms back into the bulk plasma, contaminating it with impurities that radiate energy and change the plasma behavior. Over time, sputtering may result in net erosion of the plasma facing surface which can detrimentally alter the plasma properties.

The ZaP-HD device is well-suited as a platform for PMI. A significant amount of research has been conducted to characterize its plasma behavior [33] along with progressive improvements on diagnostic capabilities [11]. The ZaP and FuZE experiments share many design elements and methods of operation, providing useful references for work on ZaP-HD. ZaP-HD can produce temperatures up to 1 keV, number densities up to 10^{17} cm^{-3}, and 300 kA of current. Pinch lifetimes up to 60 μs ensure long duration plasma exposures. Previous PMI studies conducted by Forbes [13] investigated the role of plasma kinetic and thermal energy on material deformation. Boron nitride and graphite targets were placed in the pinch and a diagnostic suite used to determine plasma behavior for a variety of experimental settings. Ex-situ surface characterization methods identified changes in surface structure. Evidence of graphite sublimation was noted, and an estimate of erosion times was presented.

The work presented here examines the material of the inner electrode, in particular the tapered nose cone that forms the end of the accelerator region. Unlike previous research, the nosecone is part of the current path and not a perturbing object inserted into the plasma. Therefore, the entire pinch current is driven through this component. The ultimate objective of this research is to determine the effect of the electrode material on the plasma parameters and pinch performance, and conversely the response of the electrode to plasma exposure. In the context of fusion, the key measures for the PMI study are the heat flux and current density, representing the transfer of energy and particles between the plasma and the solid. Alternative electrode materials can then be characterized, informing the design of next generation devices.

3.1 Theory

The physical phenomena that occur at the interface between plasma and solid materials ultimately involve some form of energetic impact between ions of the plasma and atoms of the material. If the energy of the impacting particle is larger than the surface binding energy of the lattice of atoms in the solid, then an atom is released in a process known as physical sputtering [21]. Given sufficient energy, subsequent collisions can occur in a cascade of sputtered atoms. This large removal of matter can result in the formation of pits and craters. Additionally, the material temperature may be high enough to cause melting in the case of metals or sublimation of some non-metallic materials such as graphite.

The conditions of plasma exposure vary according to the location within the device and the function of the solid surface. In tokamaks, solid plates called divertors are used to protect the device from erosion damage. High energy particles that escape magnetic confinement contact the divertor, where their energy is absorbed. In doing so, divertors also remove impurities that have been eroded from the walls, along with unwanted fusion products that need to be removed. In the Z pinch, the inner axial electrode acts as a return path for the discharge current. While in the divertor, magnetic field lines are generally glancing, with a few degrees between the field lines and the solid surface, the self-generated field lines

in a Z pinch are tangential to the surface. The mechanism of transport in this situation remains uncertain, however high particle and heat fluxes have been noted [34]. Changes in surface topography on the electrode can affect current flow and severity of PMI processes. Sputtered material from the electrode entering the plasma can cause significant heat loss to the detriment of the fusion reaction. Impurities may be recycled at the plasma-wall interface as they are redeposited and subsequently sputtered again.

3.1.1 The Plasma Sheath

For any vessel containing a plasma, two regions will develop. The first consists of the plasma itself and occupies most of the space defined by the vessel. This assumes only singly-charged ions, so the ion and electron densities in this region are equal, satisfying the condition of quasi-neutrality. A thin layer of net positive charge develops adjacent to the surface of the vessel walls known as the sheath. While in reality there is no well-defined sheath edge, this model of a contained plasma is a good approximation. Ions with a sufficient energy can enter the sheath region and are subsequently accelerated through the potential into the solid surface, where the ion can cause sputtering of surface atoms, be reflected or become embedded deep in the solid.

The energy transferred to the ion depends on the bulk plasma properties. Analysis of the plasma-side of the sheath by Stangeby for the previous assumptions [34] suggests that the sound speed c_s limits the plasma fluid velocity at the sheath edge v_{se}:

$$v_{se} \leq c_s \tag{3.1}$$

The sound speed is commonly defined as:

$$c_s = \sqrt{\frac{k_B(T_e + T_i)}{m_i}} \tag{3.2}$$

where k_B is the Boltzmann constant, T_e and T_i are the electron and ion temperatures, and m_i is the ion mass. This analysis is based on the assumption of an isothermal fluid model and a particle source proportional to the number density n. Analysis of the sheath-side by Bohm [5] showed that

$$v_{se} \geq c_s \tag{3.3}$$

This expression is known as the Bohm Criterion. Consequently, the sheath edge velocity must equal the sound speed,

$$v_{se} = c_s. \tag{3.4}$$

This particular derivation relies on the assumption of a negligible ion temperature, $T_i = 0$. For a non-zero ion temperature, the Generalized Bohm Criterion applies. That is,

$$\int_0^\infty \frac{f_{se}^i(v)dv}{v^2}\, dv \;\leq \frac{m_i}{k_B T_e} \tag{3.5}$$

Here, $f_{se}^i(v)$ is the 1D ion velocity distribution at the sheath edge. Equation 3.3 is recovered for $T_i = 0$, since the integral reduces to 1, and the left hand side to $\frac{1}{v_{se}^2}$. Riemann [28] extended this generalization further, using the values $\gamma = 1$ for isothermal flow, $\gamma = \frac{5}{3}$ for adiabatic flow with isotropic pressure, and $\gamma = 3$ for 1D adiabatic flow:

$$v_{se} \geq \sqrt{\frac{k_B T_e + \gamma k_B T_i}{m_i}} = c_s \tag{3.6}$$

3.1.2 Erosion Mechanisms

Erosion of solid materials in contact with plasma is a result of energy transfer from impacting ions. The physical mechanisms are varied, and the dependencies typically involve the ion and surface temperatures, ion flux, angle of incidence, and the combination of ions and solid atoms. Processes may involve momentum transfer, chemical reactions, thermal effects, or some combination of these. There can also be a flux of neutrals impacting the solid surface. Fusion products such as helium and neutrons must be taken into consideration. A selection of relevant mechanisms is reviewed here.

Physical Sputtering

Physical sputtering involves the transfer of momentum between impacting ions or neutrals with the surface atoms of the solid material. The surface atoms can be ejected if the energy from these collisions exceeds the sputtering threshold energy, E_{th}. This threshold energy is often estimated with the surface binding energy, E_B, that holds the atoms together. This is typically taken to be the heat of sublimation [34]. Table 3.1 lists the values of E_B for typical wall elements.

Element	**Heat of Sublimation E_B (eV)**
Lithium	1.67
Beryllium	3.38
Carbon	7.4
Iron	4.3
Molybdenum	6.9
Tungsten	8.8

Table 3.1: Heat of sublimation values for typical wall elements in fusion devices [34]. This parameter is used as an estimate of the threshold energy for sputtering.

Any kind of momentum transfer is sensitive to the masses of the belligerent objects. This is represented as an energy transfer factor γ, defined as:

$$\gamma = \frac{4M_1M_2}{(M_1 + M_2)^2} \tag{3.7}$$

M_1 and M_2 are the masses of the impacting ion and surface atom respectively. The threshold energy can then be expressed in terms of this factor:

$$E_{th} = \frac{E_B}{\gamma(1-\gamma)} \tag{3.8}$$

All sputtering processes can be quantified by the sputtering yield Y, which is simply the ratio of ejected particles to impacting particles. The physical sputtering yield will increase up to a certain impact energy, beyond which the yield decreases due to excessive penetration

of the particle into the solid, reducing the energy transferred to the surface atoms that are involved in sputtering. In general, the threshold energy is higher for heavier atoms, however the species of impacting ion may lower the threshold energy. Using the values for hydrogen ions and carbon, the threshold energy for physical sputtering is 36 eV, while physical sputtering of tungsten by hydrogen ions begins at 417 eV.

Physical sputtering is also dependent on the angle of incidence. For an angle α_0 where 0 degrees is normal to the solid surface and 90 degrees is a grazing collision, sputtering yield increases up to approximately 75 degrees [21]. Beyond this angle, reflection begins to dominate, resulting in lower energy transfer to surface atoms. The effect of a rough surface may be thought of as a change in the local angle of incidence. For example, greater sputtering yield is observed for a rough surface at a nominal angle of 0 degrees because of the large local α_0 at the peaks and troughs of the rough surface. Similarly, a smooth surface presented at a large nominal angle reduces sputtering yield because the impacting ions are actually grazing the surface. Rough surfaces are the norm rather than the exception in fusion devices, if not before plasma bombardment than almost certainly after.

Chemical Sputtering

Chemical sputtering occurs when energetic ions are involved in chemical reactions with surface atoms. As such, the specific combination of ion and surface atom is an important dependency. Chemical sputtering of carbon due to hydrogen is a key interaction for fusion devices and will be relevant for studies using the graphite nose cone. There is a strong dependence on the surface temperature, so diagnostic techniques such as pyrometry will be useful in characterizing this process. Unlike physical sputtering, there is no threshold energy for chemical sputtering, but experimental measurements suggest a peak in methane yield for a solid surface temperature around 700 K and impact energy of 100 eV [26]. The atomistic processes involved in hydrocarbon formation are complex and well detailed by Kuppers [24]. Carbon is highly preferred in fusion devices due to being a low Z element. Because of this, its presence in the core of a fusing plasma will cause less radiation cooling compared to a

higher Z element such as tungsten or copper. Graphite is commonly used due to its low cost, machinability, and good electrical and thermal conductivity.

The carbon that enters the plasma will eventually redeposit on some solid surface facing the plasma. This deposited layer can retain tritium which can accumulate, raising safety concerns and removing it from the fusing plasma. The released carbon can also be ionized and impact the surface in a process known as self-sputtering. This self-sputtering is particularly damaging due to large momentum transfer between similar masses, and can raise the sputtering yield beyond unity [34].

Melting and Sublimation

Metals such as tungsten are often used in fusion applications due to their high melting point and good thermal conductivity. However, macroscopic melting is often observed, leading to significant mass loss. Tungsten limiters on the T-10 tokamak experienced high levels of melting and erosion, along with formation of small craters for high heat fluxes [7]. The use of a graphite nose cone avoids this issue because graphite sublimates. Graphite sublimation has been measured between 3895 and 4020 K [1], higher than the melting point of tungsten. The resulting vapor consists of crystalline particles that support thermal conduction from the surface [1], which may not be possible in the case of molten droplets of tungsten. However, radiation enhanced sublimation effects can occur at sufficiently high temperatures that are still below the graphite sublimation temperature, resulting in exponential increase in erosion yield [21].

3.2 Nose Cone Material Study

An ideal material for an electrode must have several attributes. It must withstand a high thermal load, have a high melting point, high thermal and electrical conductivity, withstand ion bombardment, minimize sputtering, and be easily machined. Materials in fusion devices should have resistance to neutron damage and activation. Tritium retention solid materials is a safety concern due to its radioactivity. There are several materials that are commonly used

around fusion plasmas that meet several of these demands. Copper and tungsten are metals that are often used as plasma-facing surfaces in fusion devices. In fact, tungsten has the highest melting point of all metals, at 3,400 degrees Celsius [2]. Installing components made of high-Z materials generally reduces the tendency to sputter due to the high threshold energy associated with ejection of an atom from the lattice structure. However, other factors such as the incidence angle, surface roughness, and impacting ion-surface material combinations may preclude the use of tungsten [21]. Copper has the superior electrical conductivity, but is more prone to erosion damage. Other promising materials include various alloys [25] that seek to combine the preferred properties of both materials, and metal foams [27] due to their ability to persistently present a complex surface geometry to the plasma. This results in trapping of emitted particles in the foam cavities, reducing the sputtering yield.

3.2.1 Materials on ZaP-HD

The inner electrode of the coaxial configuration is a hollow copper tube with a 4 inch outer diameter. As shown in Figure 2.1, the electrode is tapered at its downstream end, forming a rounded nose cone. The nose cone is separate from the rest of the electrode and is threaded directly into the tube. The gap between the mating surfaces of the nosecone and the tube is minimized in order to have an uninterrupted surface. The nose cone and the tube are made from C11000 alloy copper coated with a tungsten spray 15-20 hundredths of an inch thick. Continuous operation of the device over thousands of plasma pulses has resulted in significant erosion of the surface at the tip of the nosecone. Figure 3.1 shows the extent of the degradation, where the layer of tungsten has been removed entirely, exposing the copper underneath. The area of tungsten removal is approximately one inch in diameter. The copper is marred by pits and craters, increasing the roughness of the surface. At the boundary of the exposed copper region, large droplets of molten tungsten are apparent. The droplets decrease in size further away from the nose cone tip, indicating a more energetic environment at the point of pinch current attachment.

Similar erosion damage has been observed on the copper nose cone used on the FuZE de-

vice. The performance of the FuZE plasma is much greater than ZaP-HD, with at least twice as much pinch current (see Table 1.1). Further upstream on the inner electrode, pitting has been observed at the junction of the copper tube with an alumina insulator on both FuZE [9] and ZaP-HD. The tungsten-sprayed copper nose cone on FuZE was eventually replaced with one made from POCO AXF-5Q graphite. POCO graphite is of high density due to its low porosity, improving physical and mechanical qualities. It is also highly isotropic, facilitating analysis and experimental control. Qualitative observations of the FuZE nosecone over hundreds of pulses showed considerably less material erosion without a significant reduction in pinch performance. Graphite also has the added benefit of being a source of carbon used in spectroscopic measurements, eliminating the need for operating with a mixture of gases to seed the carbon impurity.

Figure 3.1: The tungsten-sprayed copper nose cone during disassembly of the ZaP-HD device. The tungsten at the tip has been completely eroded, exposing the bare copper underneath.

Figure 3.2: The region of tungsten erosion is approximately one inch in diameter. The copper surface has been roughened by the pits and craters that have formed. Molten tungsten cooled and formed droplets which can be seen at the periphery of the exposed copper. The size of the droplets decreases away from the tip.

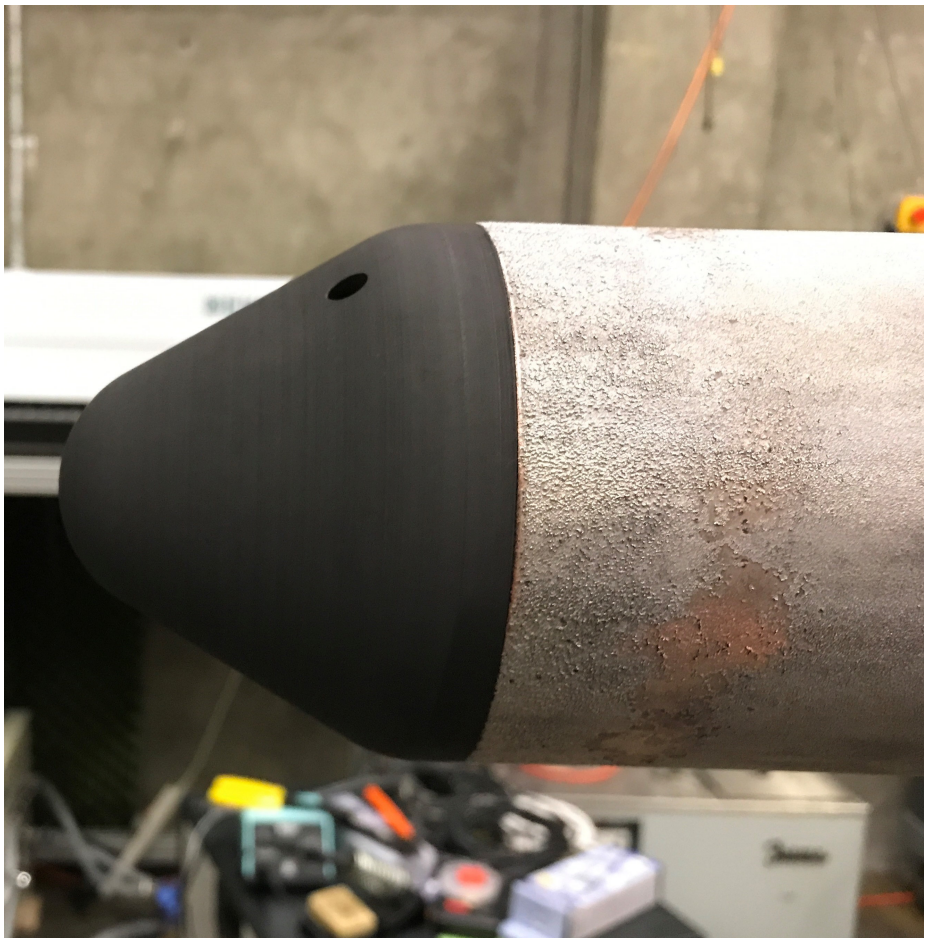

Figure 3.3: The graphite nose cone fully threaded into the inner electrode.

3.2.2 Removable nose cone design

Characterization of the graphite nose cone is necessary for future PMI studies. In order to make measurements of surface topography, material samples must be placed in an ex-situ device. The large size of the nose cone and the extensive process of removal make it unfeasible for surface measurements. Therefore, a portion of the nose cone will be removable. A section-view of the design is shown in Figure 3.4. The nose cone has been divided into two components, a graphite base portion, and a removable tip. The tip of the nose cone is fixed by axially aligned bolts. Access to the nose cone is typically achieved by removing the entire inner electrode. With this design, the removable tip can be accessed through one of the rectangular viewing windows in the assembly region. Removal of the windows requires bringing the vacuum chamber up to atmospheric pressure, a process which can be completed in less than an hour. Before implementation of this design, a basic graphite nose cone without the removable tip provides baseline performance and erosion characteristics. In subsequent studies, the removable tip may be manufactured from alternative materials such as copper-tungsten alloys, or sprayed with a thin layer of test material. Similar PMI experiments have been conducted on DIII-D [29] using a graphite sample holder to study sputtering erosion, re-deposition and movement of high-Z elements in the divertor. Samples consisted of metallic coatings on graphite inserts, allowing for net erosion and surface topography measurements.

3.2.3 Pinch Characterization

There are two components of the PMI study: pinch characterization and material characterization. The first addresses the question of how the inner electrode material affects the plasma parameters and the pinch performance. The general method of determining the characteristics of the pinch has been detailed in Chapter 2.3. Spectroscopy chords are positioned at the tip of the nosecone by sliding the telescope along the window rail, providing measurements of the ion temperature. Spectroscopy is also used to identify impurity species in the plasma. While the graphite will only sputter carbon, there are numerous other impurities that may

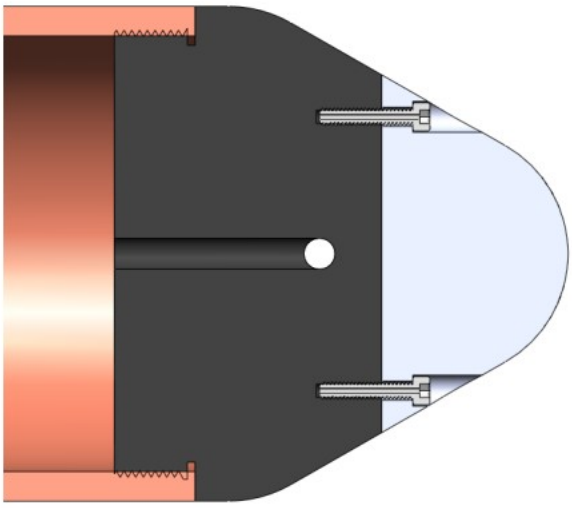

Figure 3.4: Cross-section view of the PMI nose cone design. The overall geometry is identical to the original design, with the graphite portion threading directly into the copper tube. The removable tip is fixed by two axial bolts. The tip material allows ex-situ analysis of surface topography and can be used to test different materials.

be present in the plasma from erosion of the tungsten-sprayed copper, boron nitride shields of the magnetic probes, outgassing from the vacuum chamber walls, or from extended exposure to ambient air. Establishing a background level of impurities is essential for analysis of different materials, and to estimate energy radiation from the different impurity species. Lastly, the Kirana camera can be angled slightly upstream to directly image the nose cone and capture the current attachment along with the pinch. In general, it provides visual information of pinch stability to compare to diagnostic measurements. The dual view through the periscope apparatus provides a top-down and side view of the plasma.

3.2.4 Material Characterization

Material characterization will involve measuring the total erosion of the graphite nose cone across a few hundred discharges. This is done by a simple weight-loss measurement performed prior to installation and after removing the nose cone. The profile of the entire nose cone was measured immediately after manufacturing and reproduced in Figure 3.5. The entire nose cone is too large to be analyzed completely by a scanning electron microscope or profilometer, so a basic measurement was done using the digital read out on a CNC lathe. A dial indicator mounted on the tool holder was used to contact the nose cone surface every quarter of an inch along the z-direction. This measurement was repeated after rotating the nose cone 90 degrees for four sets of data. Because it is unlikely the same reference point will be used after plasma exposure, multiple measurements allows an average to be calculated. The vertical axis, X, shows the indicator measurement relative to the largest diameter of the nose cone. At this reference location, the radius $r = X + 2$. The points are the average of the four measurements, while the red line is a spline fit of the average points. The purpose of the fit is only to visualize the profile defined by the points. This measurement will be repeated after plasma exposure to identify locations of material loss. Measurements beyond Z = 3 were not taken due to limitations of the indicator tip. The removable tips will be analyzed using ex-situ diagnostics described in Section 3.4.

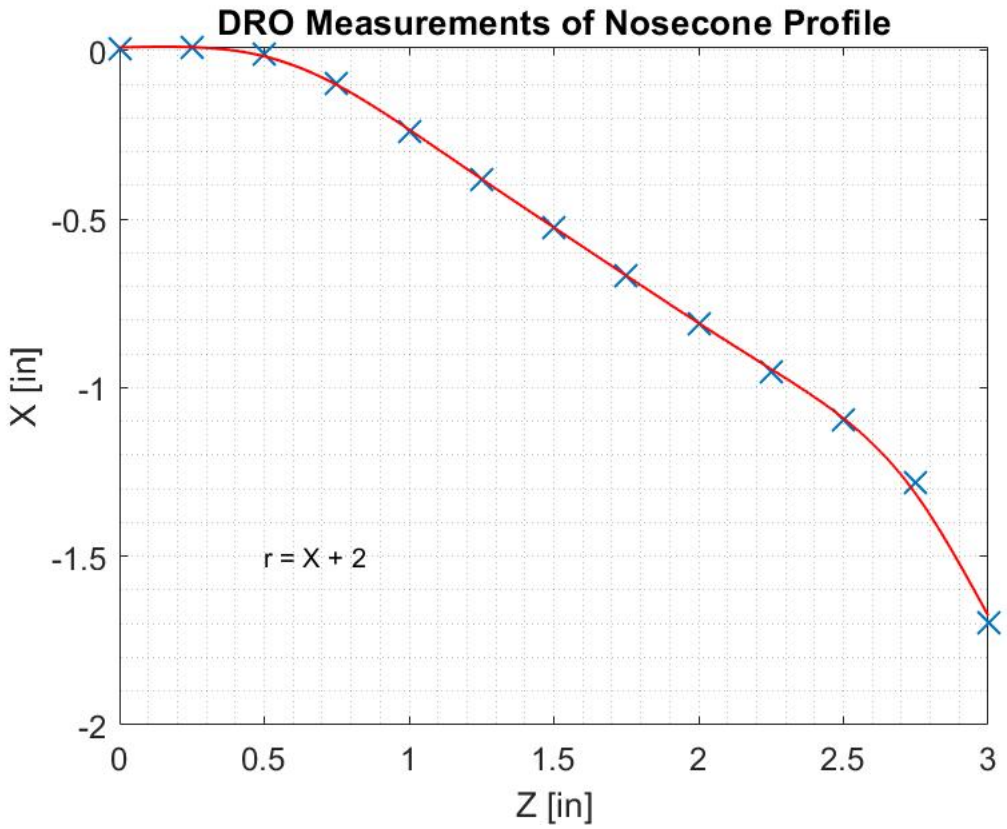

Figure 3.5: Measurements of the graphite nose cone profile using the Digital Read Out (DRO) on a lathe. A dial indicator is mounted onto the tool holder and is used to contact the nose cone surface at multiple locations in the z-direction. The radius is given by $r = X + 2$. The crosses represent the average of four measurements taken at azimuthal locations 90 degrees apart. The red trace is a spline fit of the average points to visualize the nose cone profile.

3.3 Experimental Parameters

Several different experimental parameters were varied to characterize the graphite nose cone. The charge voltage of the capacitor banks ranged from 3 – 9 kV. In the accelerator, the energy discharge goes into the kinetic energy of the particles. The compression bank discharge provides additional current that goes into heating and compressing the plasma in the assembly region. This increases the thermal energy of the plasma. Therefore, variation of the charge voltage is a method of controlling the form of energy imparted to the plasma.

The acceleration bank was set to trigger at t = 0 for each pulse. The compression bank is delayed a certain amount of time after this initial trigger to allow the plasma to travel along the accelerator and enter the assembly region. Insufficient plasma in the accelerator at the time of compression bank discharge can result in damage to the electrodes because the plasma completes the path for the high current density to pass through. The compression bank delay timing was varied between 20 and 30 us to determine a suitable timing that resulted in greater pinch stability, along with brighter and more uniform C-III signals for spectroscopy.

Unlike the magnetic field, current, and voltage diagnostics in use, the ion Doppler spectroscopy setup is not time resolved. Replacing the ICCD detector in the spectrometer with the Kirana allowed for time-resolved spectroscopy measurements [11], however the use of the Kirana viewing the side window precluded this capability. While light is constantly being collected by the telescopes and optical fibers throughout the pulse, the amount of light exposure to the ICCD can be controlled. The exposure trigger time, gate width, and gain were controlled via the spectroscopy operating computer. A time resolved profile of ion temperature may be obtained by triggering the ICCD over consecutive time increments, however this would require a significant number of pulses. A typical gate width of 1 us was used, and the trigger time was set to 45 and 55 us. These times straddle the time of peak pinch current and plasma current in order to capture light during the most stable period of the pinch. Spatial resolution was obtained by translating the telescope downstream along the

window rails. Data presented here was taken at P0 and P15.

3.4 Surface Analysis Tools

Analysis of surface topography is an essential aspect of understanding the material response to plasma bombardment. The processes described previously often leave features on the nanometer to micrometer scale. These can include eroded and deposited layers, craters, and droplets of molten metal. The thickness of deposition and depth of erosion can be quantified and compared to expected yield calculations. Elemental analysis of deposition layers and other features identifies the species involved. Quantifying changes in surface roughness is useful in determining sputtering behavior, which is dependent on the local incidence angle. Ex-situ surface analysis provides a method of comparison before and after plasma exposure. Methods also exist that provide these measures during exposure, such as in-situ microscopy for temporally resolved sputter erosion [27]. Mass spectrometry has been used to measure rates of hydrocarbon impurity formation [26], though this may be difficult to implement on ZaP-HD. The ex-situ analysis tools that will be used are presented in the following sections.

3.4.1 Optical Profilometry

A profilometer or profiler is an instrument that quantifies roughness by measuring the surface profile. Contact profilometers achieve this by the motion of a physical stylus across the surface of a sample, where the deflection of the stylus can be converted into a depth measurement. Non-contact profilometers, often optical systems, measure the interference patterns of two beams of light. The first beam acts as a reference and the other is reflected off the sample surface. Optical profilers are fast, non-destructive, but limited in resolution by the diffraction limit. The dome-shaped area of interest on the removable tips shown in Figure 3.4 is well-suited to the capability of the optical profiler due to the large vertical translation required. A scan of the entire curved surface with a contact profiler would require extensive adjustments that are out of the range of motion of the stylus, and risk damage to the device and sample.

An Olympus OLS4100 optical profiler is provided by the UW Clean Energy Testbeds (CET) facility. Lateral (x and y) resolution and vertical (z) resolution can reach 10 nm. This model can also image sloped surfaces up to 85^o. An image of the entire dome would decrease resolution to more than 1 micron. Therefore, smaller areas of interest will be scanned separately to maintain high resolution. The OLS4100 is a confocal digital microscope that uses a laser as its imaging beam. Confocal systems focus the light source in a precise location to eliminate signals from out-of-focus light. While this requires a scan to cover the desired area of measurement, the gains in optical resolution are significant. Relevant outputs from the optical profiler are surface roughness values, volumetric measurements above or below a threshold (deposition or erosion post-plasma exposure), and depth measurement of surface features.

3.4.2 Atomic Force Microscopy

An atomic force microscope (AFM) is a tool for measuring surface topography with enhanced vertical resolution. Images are generated by motion of a small cantilevered tip across the sample surface. A laser is reflected off the cantilever to a photodiode. As the cantilever bends to follow the surface profile, the change in laser signal is converted into topography information. The Jupiter XR AFM is capable of sub-nanometer resolution, making it ideal for accurate measurements of features unresolvable by optical systems. This could be useful for sputtering and redeposition measurements, although this is only achievable for small areas. AFM scans are more time-intensive than optical profilers, and incapable of measuring steep angles. Unique to the AFM is the ability to operate in one of three modes: contact, tapping, and non-contact. Contact mode is the standard mode of operation, similar in principle to contact profilometry. Tapping mode oscillates the cantilever to avoid the tip from adhering to a liquid layer that tends to form on samples in ambient conditions. The oscillation is such that the lowest point of oscillation is enough for surface detection to occur. Non-contact mode involves oscillating the cantilever at its resonant frequency and measuring the damping effect of van der Waals forces on this oscillation at certain distances above the

sample. This mode avoids the issues discussed previously with contact profilometry.

3.4.3 Scanning Electron Microscopy

Scanning Electron Microscopes (SEM) produce micrographs of the sample surface by measuring the secondary electrons emitted by atoms of the sample following electron bombardment. The signal intensity is a function of the surface topography. In general, SEMs operate by placing the sample in a high vacuum, although additional sample preparation is sometimes required. The Phenom ProX SEM is capable of sub nanometer resolution. Micrographs are typically two-dimensional, lacking the height resolution that can be obtained with the optical profiler or AFM. The main advantage of the AFM is its high resolution and speed which can be used over a relatively large scan area on the order of millimeters. The SEM will be used for rapid scans of the entire sample surface, and to identify locations for elemental analysis.

3.4.4 Energy-Dispersive X-ray Spectroscopy

Energy-Dispersive X-ray Spectroscopy (EDS) is often equipped to a SEM. An X-ray beam is focused onto the sample, which excites and ejects electrons in their ground state. An electron from a higher energy level then occupies the empty electron position, emitting another X-ray as a result. A spectrometer collects and sorts the emitted X-rays by wavelength, which is characteristic to the atom, enabling elemental identification. In micrographs obtained for samples of graphite used in testing by Forbes [13], droplets of tungsten were identified using EDS and shown in Figure 3.6. EDS is able to calculate the percentage of each element measured. In this micrograph, 12.27% of the sample was tungsten, with carbon making up the rest of the sample.

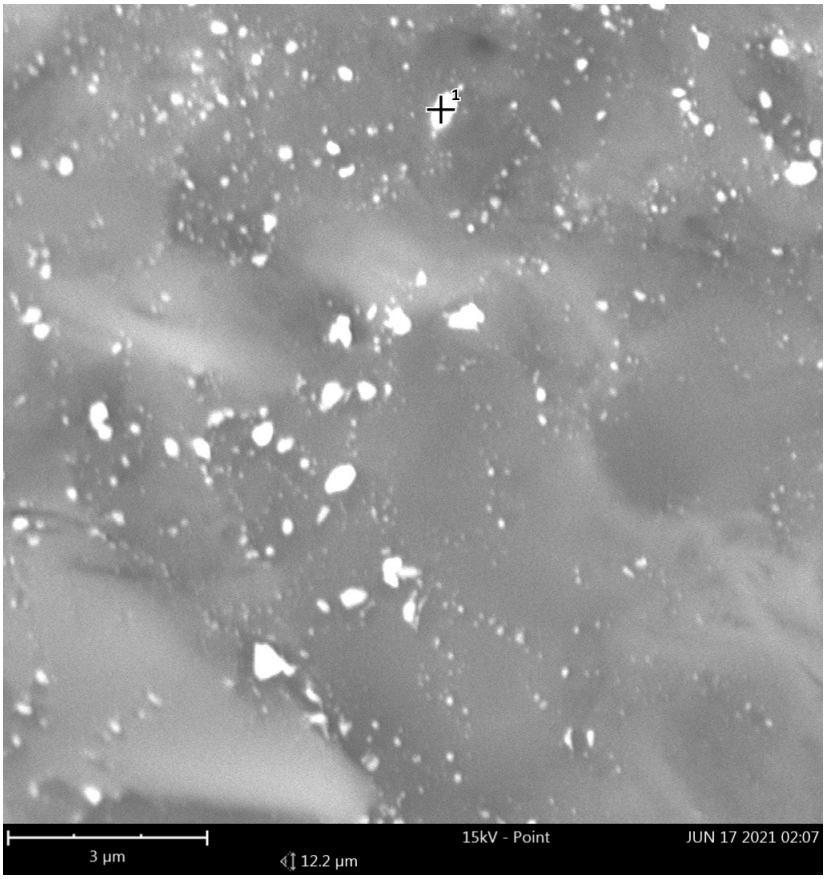

Figure 3.6: SEM micrograph of a graphite target exposed to ZaP-HD plasma from work by Forbes [13]. Field of view spans 12.2 microns. The scattered white objects are identified as tungsten using EDS, amounting to 12.27% of the imaged atomic concentration.

Chapter 4

EXPERIMENTAL RESULTS

The ZaP-HD device has a wide range of operational parameters that may be controlled. The run campaign involving the graphite nose cone sampled a selection of these parameters in order to determine the effect of the graphite nose cone on the pinch performance. Table 4.1 lays out the range of conditions used for this characterization. In total, 236 plasma pulses were taken over the course of several weeks. The plasma current increases with the power supply charge voltage, increasing the plasma parameters. Because a long-lived, stable pinch is desirable to maintain plasma bombardment for materials characterization, the quiescent period duration was studied for a set of pulses. It is also necessary to verify a reproducible discharge for a range of settings. This is to ensure control of plasma exposure to the solid material for a repeated set of identical pulses. In addition, the timing and location of the telescope for spectroscopy were also varied. A temporal and axial resolution of ion temperatures is useful for characterizing the time and location of high energy density conditions. A limitation of the existing diagnostic suite is the inability to measure impurity concentrations or sputtering yields, which would be key PMI-relevant quantities to monitor during operation.

Parameter	Value
Gas	Hydrogen
Charge Voltage (kV)	1 - 9
Compression Bank Delay (μs)	20 - 30
ICCD Trigger (μs)	45, 55
Spectroscopy Axial Location	P0, P15
Inner/Outer Gas Valve Pressure (Torr)	3400/3300
Inner/Outer Gas Valve Timings (ms)	-1.4/-0.8

Table 4.1: ZaP-HD operational parameter ranges used in the graphite characterization run campaign.

4.1 Variation of Charge Voltage

One of the simplest parameters to vary is the charge of the dual power supply. The energy discharged from the acceleration bank goes into ionization of the neutral gas supply and kinetic energy of the plasma. The compression bank energy is converted into thermal energy of the plasma by ohmic heating from the discharge current. Experimental operation begins with an incremental increase of the charge voltage up to the desired values, beginning at $[V_C,V_A]$ = [1,3] kV and ending at [7,9] kV. V_C and V_A are the compression voltage and acceleration voltage respectively. A single repetition of the pulse was taken at each voltage setting. The pinch current at P0 increases consistently with a 1 kV increment in compression and acceleration charge voltages, as plotted in Figure 4.1. The pinch current surpasses the 50 kA mark for a charge of [4,6] kV, and nearly reaches 100 kA for [6,8] kV.

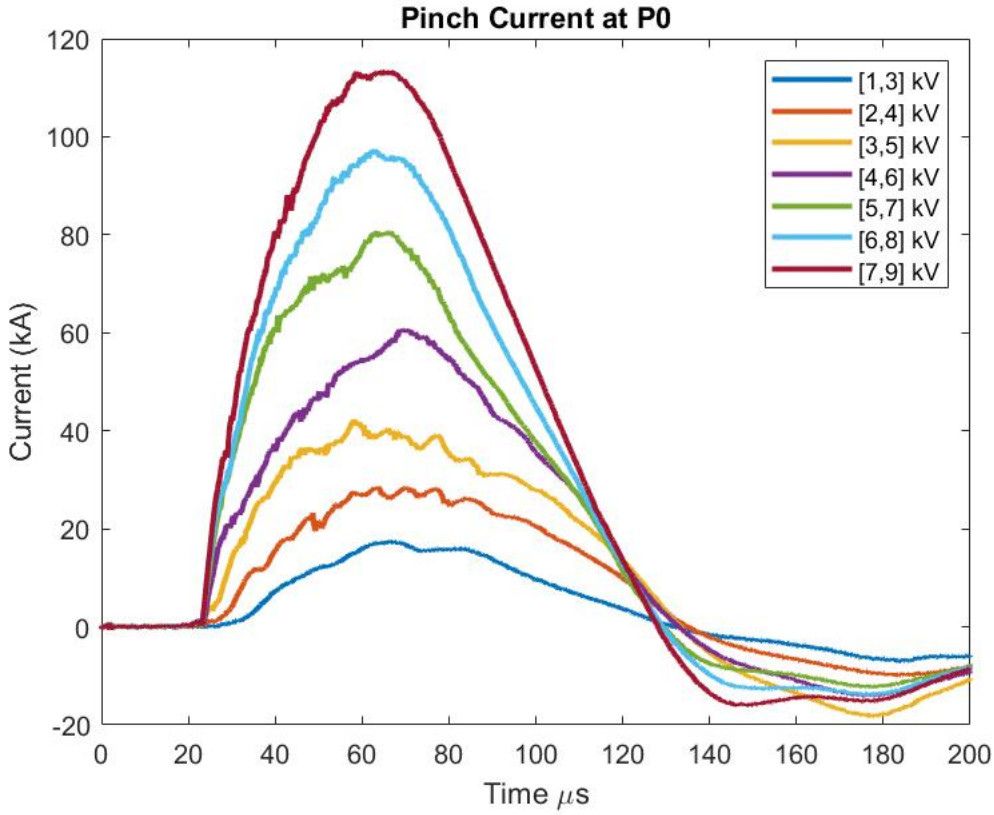

Figure 4.1: The pinch current measured at P0 increases consistently as the charge voltage, [V_C,V_A] kV, of the power supply capacitors increases. Data are from pulses 210721002 - 210721015.

A quiescent period defined by the normalized m_1 mode is observed at voltages at or above [4,6] kV. Of the two pulses at this setting, the longer quiescent period was 35 μs. At the highest voltage setting of [7,9] kV, the longest period increased to 50 μs, while 60 μs was observed for [6,8] kV. Given the small sample size, it is too early to tell if there is an optimum voltage setting beyond which quiescent periods decrease. This inconsistency likely reflects the variability between pulses rather than the existence of an optimization. Despite this, this voltage scan is useful to show general operating trends and to confirm machine functionality.

Figure 4.2 shows the ion temperature measured from the Doppler broadening of the C-III impurity line for increasing voltage. The temperature is calculated for each fiber chord in the bundle. The bars represent a 95% confidence interval. No consistent trend is evident from the plot, although the temperatures for chords 10 and above at [7,9] kV are slightly higher than at lower voltages. Measurement of Doppler broadening from C-V may be required to observe higher temperatures. The plot shows a curved profile, where the edge chords corresponding to chord numbers below 10 have a higher temperature, but large interval bars. The lower chord numbers show a wider variation in temperature, but inconsistent with increasing voltage. If the chord-averaged temperature is calculated for each voltage setting, there is an increase in the measured ion temperature of from 95 to 98 eV between [3,5] kV and [7,9] kV. It is expected that increasing the compression bank charge voltage should increase the ion temperature due to a greater pinch current as seen in Figure 4.1. However, this increase is within the interval bars plotted, therefore too small to represent a real trend in data.

Referring back to Figures 2.8 and 2.9, the fitted Gaussian profile for the lower chord numbers is wider than the larger chord numbers, resulting in a large temperature. However, one would expect a hot plasma core in the center of the pinch, evidenced by higher intensity in the central chords in Figure 2.5. The central chords show the lowest temperatures and the smallest interval bars. The central chords also show little variation with adjacent chords, compared to the large gradient in measured ion temperature from edge to center chords. This

suggests that a more uniform light intensity is incident on the central chords compared to the edge chords, resulting in more consistent Gaussian profiles. With this in mind, the central chord temperatures can be used as a value for comparison along with the chord-averaged value. In this case, the variation across the range of charge voltages is larger, from 58 to 67 eV for the same voltage range.

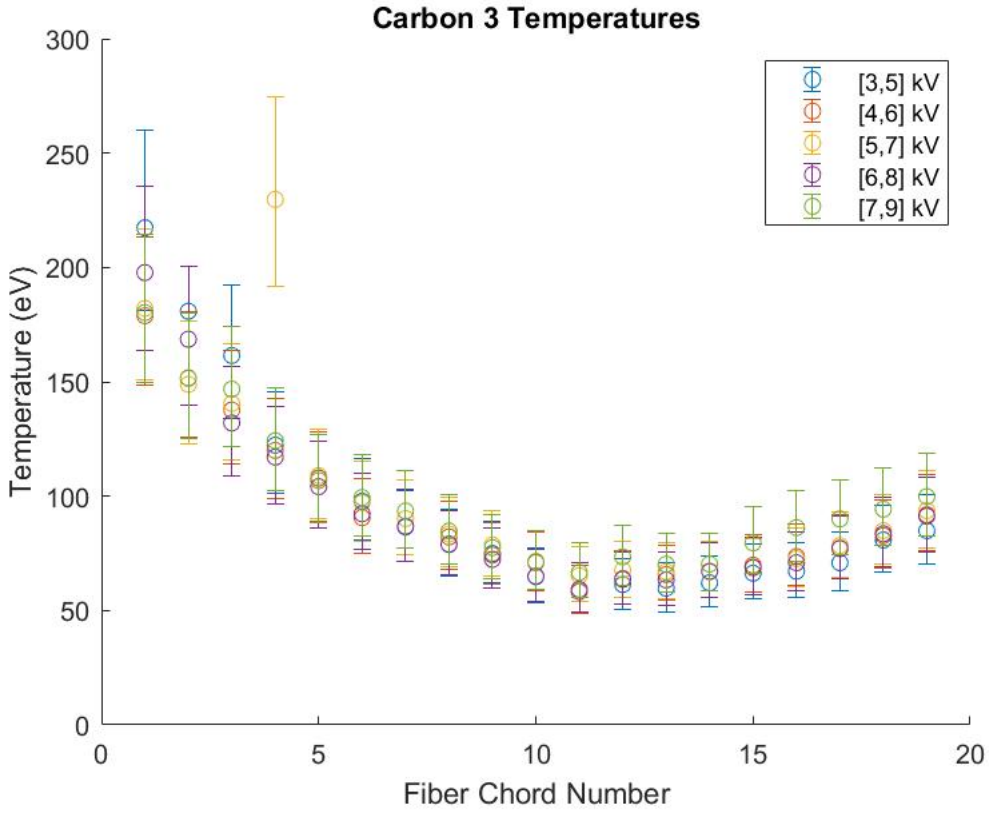

Figure 4.2: Ion temperatures measured from the Doppler broadening of the C-III impurity line at 229.7 nm, calculated at each chord in the wide fiber bundle. Data is plotted for five pulses: 210721006, 210721008, 210721010, 210721012, and 210721015 respectively with increasing voltage. Not enough light is collected for pulses below [3,5] kV to register a useful spectrum. There is a slight increase in the chord-averaged ion temperature with charge voltage, however no clear trend is evident from the plotted data.

A coherent pinch was visible on the Kirana for [4,6] kV charges and above. Figure 4.3 shows four Kirana frames for pulse 210721015, taken at [7,9] kV. The four frames span roughly one microsecond, and the pinch current at P0 is approximately 100 kA. The periscope view of the top window appears at the top of the image, and the side window appears at the bottom. The periscope image is limited to the 18 centimeter length of the mirrors. The side window extends through the assembly region. In Figure 4.3a, the pinch is well-formed and very bright in both views. A vertical kink is visible in the side view and a lateral kink in the top view. About 0.3 μs later in Figure 4.3b, the instability is still visible. In Figure 4.3c, the top view shows a disruption in the pinch, although the entire structure remains intact. In Figure 4.3d, the disruption in the top view has caused significant deviation of the plasma inwards from the radius maintained upstream. In the side view, the plasma takes on an asymmetric shape.

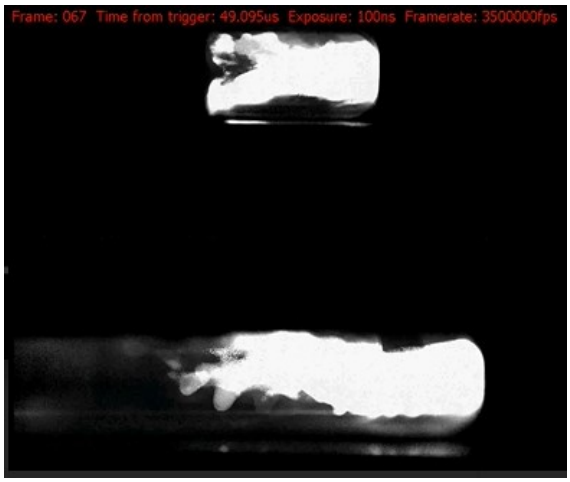

(a) 49.095 μs

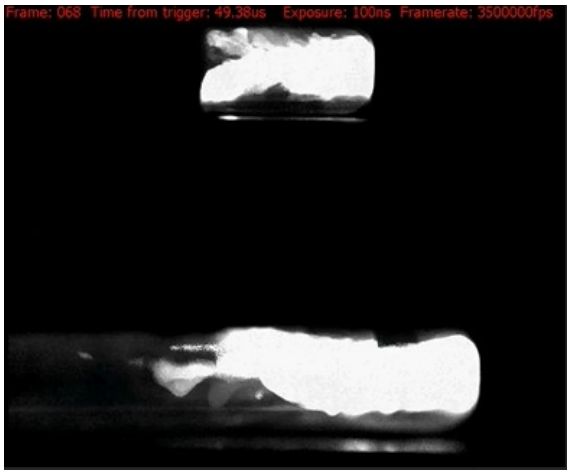

(b) 49.38 μs

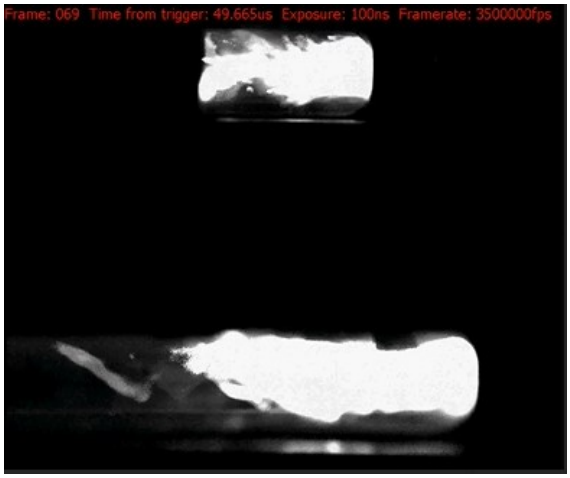

(c) 49.865 μs

(d) 49.95 μs

Figure 4.3: Individual frames from a Kirana recording for pulse 210721015 at 7 kV compression voltage and 9 kV acceleration voltage. The total duration over the four frames is approximately 1 μs. The periscope view of the top window appears at the top of the frames, and the image through the side window appears at the bottom. The pinch has a well-defined radius, but a kink instability persists for the first two frames. A disruption is visible downstream in the last two frames although the pinch remains intact just upstream.

4.2 Variation of Compression Bank Delay

For each pulse, the acceleration bank is the first of the two power supplies to discharge. This occurs at $t = 0$, and the compression bank discharge is delayed to coincide with the arrival of plasma in the assembly region. A set of pulses was taken with the compression bank delay varying between 20 and 30 μs. A constant charge voltage of [6,8] kV was used. The plots in Figure 4.4 show the mode and current data for a selection of these pulses. The plasma current has a distinct increase after the compression bank discharge and for a non-zero m_1 mode. This confirms that there is plasma in the assembly region at the time of compression bank discharge. Following the plasma current rise is a rapid decrease in the mean m_1 mode and increase in the pinch current as the plasma forms into a column. During this time, large current oscillations associated with the discharge may cause the mode data to increase above the threshold, seen between 30 and 40 μs in Figure 4.4b. In general, the value of m_1 during the quiescent period appears insensitive to the compression delay, however earlier delay times resulted in fewer oscillations during peak current. Figures 4.4c and 4.4d show more variation in the mode data that crosses the stability threshold. Consequently, stability is very short-lived. For longer delays, there is a significant decrease in mean m_1 prior to the quiescent period. This is apparent just before 30 μs in Figure 4.4d. This decrease happens for shorter compression delays but is less pronounced. Too late of a compression discharge means more of the plasma has already traveled downstream of the nose cone, where attachment occurs for the pinch current. Downstream plasma can make contact with the walls of the assembly region and cool down enough for recombination, reducing the plasma supply.

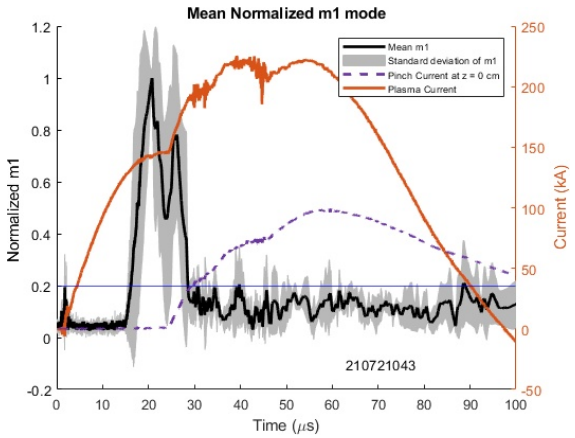

(a) 21 μs delay

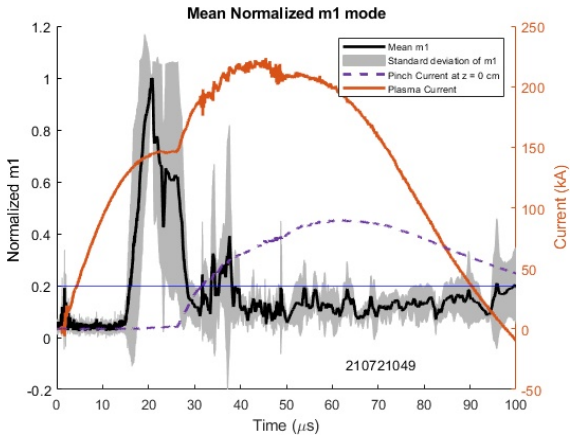

(b) 24 μs delay

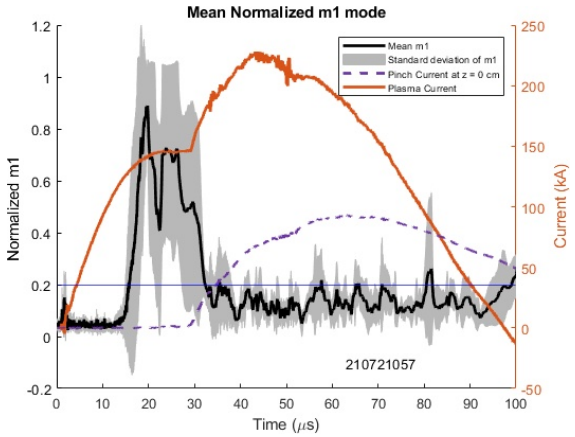

(c) 27 μs delay

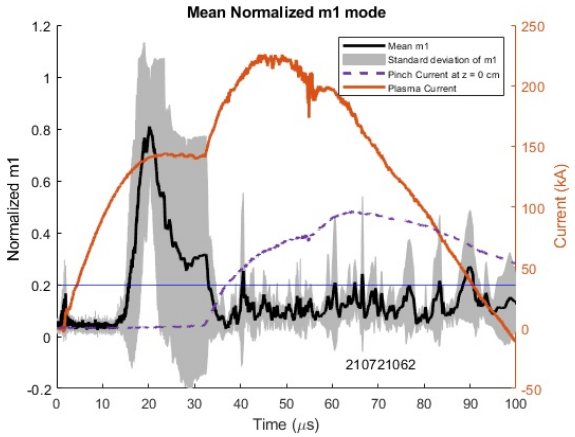

(d) 30 μs delay

Figure 4.4: Combined plots of mean normalized m_1 data, plasma current and pinch current at P0. Gray infill represents the standard deviation of the mode data. Each plot shows a different compression bank delay time. The value of the mean m_1 appears insensitive to the compression bank delay time, but shorter quiescent periods are observed for longer delays due to decreased stability.

Figure 4.5 plots the estimated quiescent period for each of the delay times for pulses 210721041 - 210721062. Quiescent periods appear to increase up to a delay of 24 μs. For longer delays, the quiescent period duration drops precipitously, due to the m_1 oscillations discussed. There are no data points at 23 and 26 μs due to insufficient data. Since two pulses were taken at each setting, the pulse with the longer quiescent period was selected. The single pulse repetition at each delay time showed variability in the pinch behavior. For example, large transient oscillations in current that raised the mode data above the quiescent threshold. Recalling the formation of instabilities from Section 1.3, localized regions of increased magnetic field form from small perturbations which act to increase the perturbation. This movement of the plasma causes disruptions of the current. Because of the variability, a larger number of repetitions is required to reduce the effect of these transients and to verify this trend in stability with compression delay.

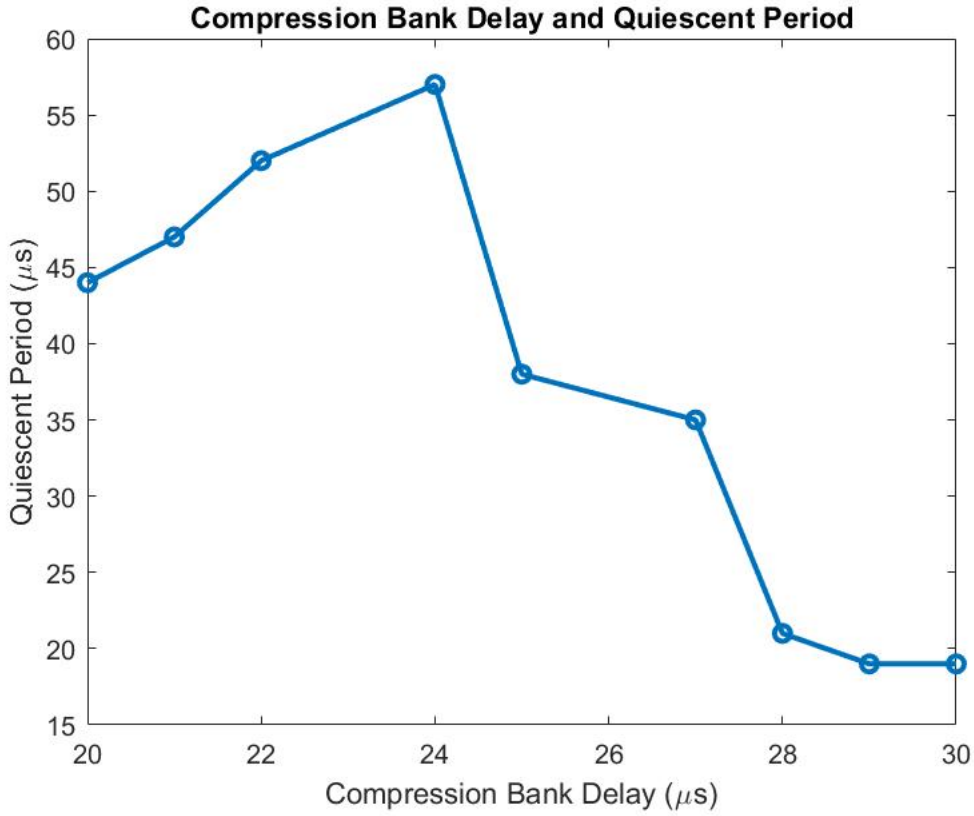

Figure 4.5: Estimated quiescent periods for a set of pulses with increasing compression bank delays. The longest duration is 57 μs for a 24 μs delay. As the delay moves later into the pulse, disruptions in the plasma cause the m_1 mode to increase above the quiescent threshold. The quiescent periods drop to below 20 μs. This decrease is associated with plasma moving too far downstream to be involved in pinch formation. This plot uses data from pulses 210721041 - 210721062.

Ion Doppler spectroscopy measurements were taken for the same set of pulses. The ICCD was set to trigger at 50 μs throughout this set of pulses. The exposure time was 1 μs, gain was 150, and light was collected through the wide fiber bundle on the oblique telescope viewing P0. A direct comparison of the measured temperatures from C-III emission for 20 and 30 μs compression delays is shown in Figure 4.6. The longer delay resulted in higher temperatures for lower chord numbers, while they are very similar on the other side of the bundle. As seen previously, the size of the confidence interval bars is smallest at the center of the chord bundle.

The ion temperature from the C-III impurity is presented in Figure 4.7 as the central chord value and the chord-averaged value. Because of the higher temperatures calculated from the edge fibers and outliers, the average difference in the two temperature definitions is 32 eV. Due to this effect, the value of the central chord is the more reliable quantity for consideration. For compression delays up to 28 μs, the center chord temperatures are fairly consistent. The increased values at 29 and 30 μs delays may be related to changes in the pinch current seen in Figure 4.4 at 50 μs. The pinch currents are reproduced in Figure 4.8. There is a distinct oscillation that occurs just before the maximum for all three delay times. The severity of the oscillations is reduced for the 20 and 30 μs delay. For the 30 μs delay, there is a steeper rise in pinch current immediately after the oscillation, although this is well beyond the ICCD exposure time to have an effect on spectroscopy. Notably, the magnitude of the pinch current at 50 μs decreases with a longer delay, from 87 to 79 to 72 kA respectively. This is expected, since the longer delay means that peak pinch current is attained later in time. A lower pinch current should result in less confinement, but the mean m_1 mode at this time is below the threshold. As such, it is difficult to attribute the higher measured temperatures to current oscillations or reduced pinch current. Further investigation is needed with an increased data set to reduce the effects of variability between pulses.

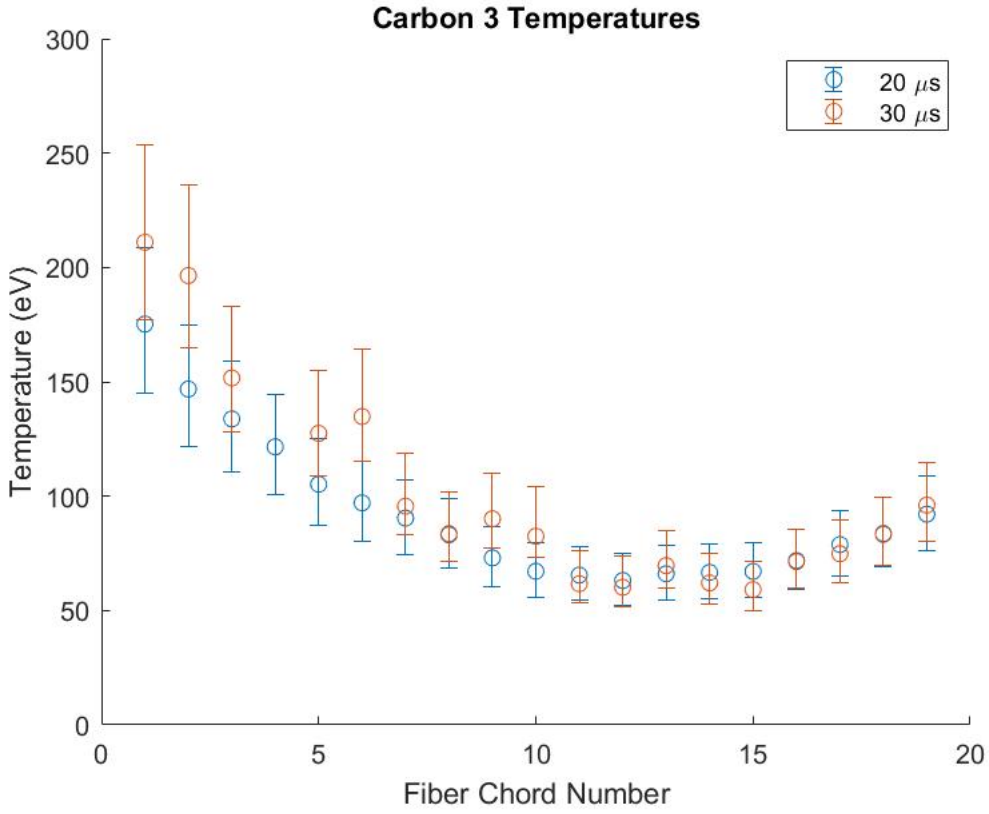

Figure 4.6: Measured ion temperatures from the C-III line for the shortest and longest compression bank delay times vary significantly for edge chords on one side of the fiber bundle. Interval bars for low chord numbers are much larger than those in the center. This could be due to differences in light intensity from oscillations in the pinch current. The temperatures at both delay times match for chord numbers above 10. Temperatures are from pulses 210721041 and 210721062 respectively for increasing delay time.

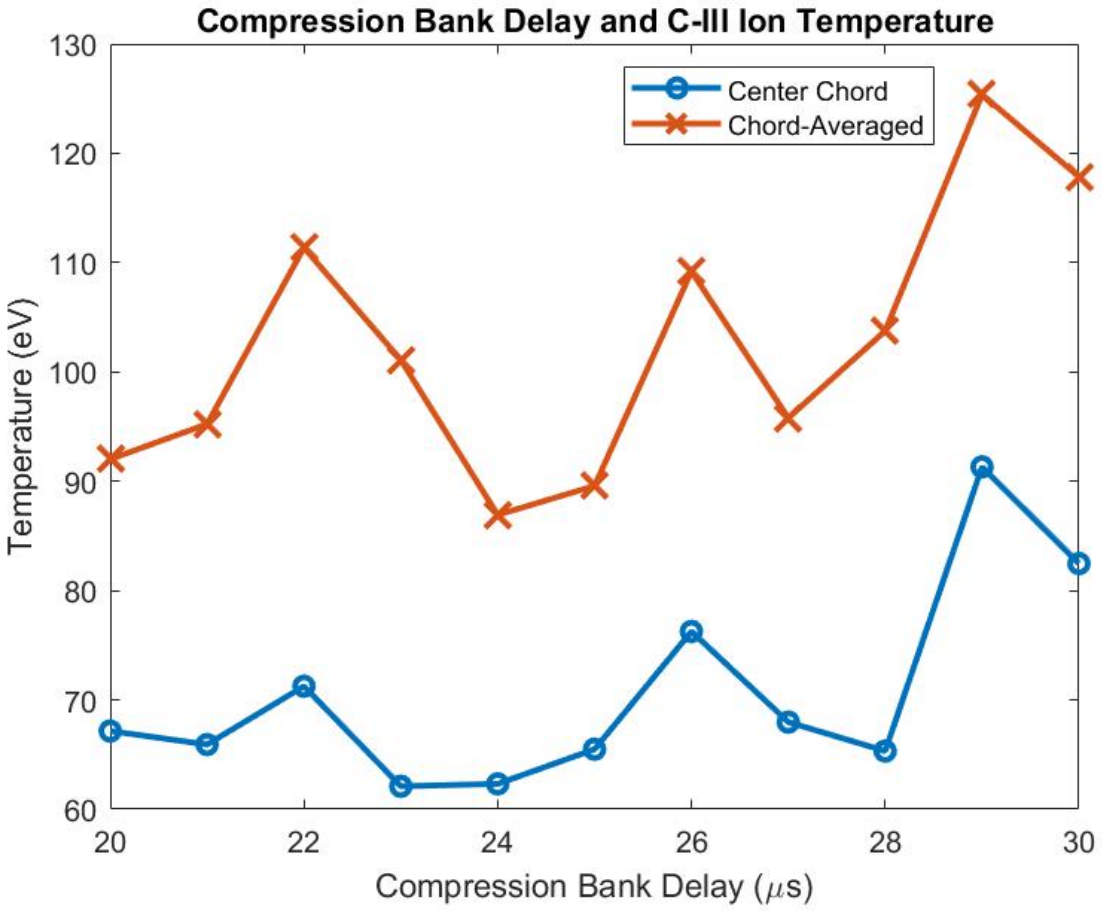

Figure 4.7: The ion temperature from C-III line emission is plotted against the compression bank delay time. Two measures of the ion temperature are considered: the value from the central chord, and the chord-averaged temperature. The former has a smaller error (see Figure 4.6) and the latter includes edge fiber effects and possible outliers which increase the average. Temperatures of the central chord remain relatively constant until a 29 μs delay time. This plot uses data from pulses 210721041 - 210721062.

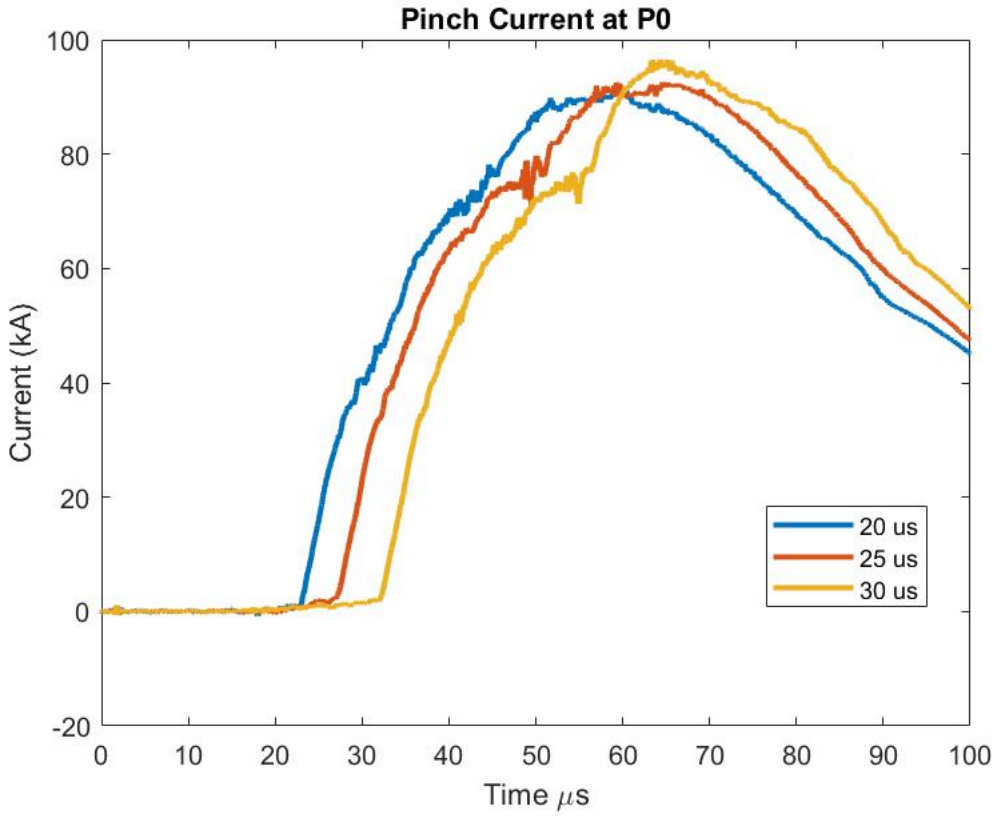

Figure 4.8: P0 pinch currents for selected pulses with varying compression bank delay times. The ICCD is triggered at 50 μs with an exposure of 1 μs. An oscillation occurs for each pulse just before peak pinch current. The magnitude of the current at 50 μs decreases with a longer delay, but the peak magnitude increases. Data are for pulses 210721041, 210721051, and 210721062 respectively.

4.3 Variation of ICCD Trigger

Given the evolution of pinch current and magnetic field discussed previously, the measured ion temperature is contingent on the time and duration of light collection. Time-resolved spectroscopy is possible with the described setup, but involves hundreds of pulses to develop an adequate data set. Due to limited weekly operation, only two ICCD trigger times were studied. The pinch current has a maximum at 50 μs for a [6,8] kV charge voltage and 20 μs compression bank delay. Two sets of 10 pulses were taken with an ICCD trigger of 45 and 55 μs to capture spectra from just before and after the time of maximum pinch current. The telescope was positioned at P0 to view light in the vicinity of the nose cone. Figure 4.9 shows the normalized m_1 and relevant currents for a representative pulse. Peak pinch current was 91 kA, and a 42 μs quiescent period occurs from 48 to 90 μs.

Figure 4.10 shows the recorded spectrum from the ICCD. All 20 chords are distinct, although the edge chords received a lower intensity of light. The central chords are fairly uniform in intensity. Figures 4.11 and 4.12 show the fitted Gaussian profiles and the resulting ion temperatures. As seen previously, there is a bowed profile to the temperature across the chords. The high temperatures correspond to the first few chords in Figure 4.10 with lower intensity, as well as the first few fits with wider Gaussian profiles. For the 45 μs ICCD trigger, the campaign-averaged ion temperature over ten pulses was 98.7 eV with a standard deviation of 8.3 eV using the chord-averaging method. Using the central chord results in 74.0 eV with 10.1 eV standard deviation. For the 55 μs ICCD trigger, the corresponding values were 100.1 $\pm$ 3.3 eV chord-averaged and 71.4 $\pm$ 4.1 eV at the central chord. Figures 4.13a and 4.13b show the distribution of data for all ten pulses at each setting. Outliers occurred frequently for the dimmer chords at the edge, while the spread decreased for the center chords. Given the relative proximity of the ICCD trigger times and similarity of campaign-averaged temperature values, it follows that there is not much difference between the two settings.

The issue of repeatability, especially in terms of chord illumination should also be con-

sidered. Several spectra were severely asymmetric, suggesting movement of the pinch which caused a non-uniform illumination of the chords. Figure 4.14 shows Kirana images of the plasma for two identical pulses and identical times. Similar to previous images, two views of the plasma were recorded. The top window was imaged through the periscope, and appear above the view from the side window. The downstream direction is to the left. The curved border between the plasma and dark background is the slot in the outer electrode. The nose cone tip is a few centimeters upstream of the slot, therefore is not in view of the Kirana. However, these images still provide useful qualitative information to compare with other diagnostics. In particular, Figure 4.14a shows a well-defined pinch, while Figure 4.14b shows almost no visible light at all. The Kirana has shown an undesirable effect of periodic oscillations in intensity, where the images appear to vanish and then return a few frames later. Further analysis is required to distinguish this effect from actual dissipation of the plasma. Conversely, Figures 4.14c and 4.14d show a well-defined pinch for both pulses and in both top and side view. The upstream end of the pinch in both images tapers down to a smaller diameter from the larger diameter at the point of current attachment with the nose cone. Comparing the side views reveals some vertical asymmetry of the plasma.

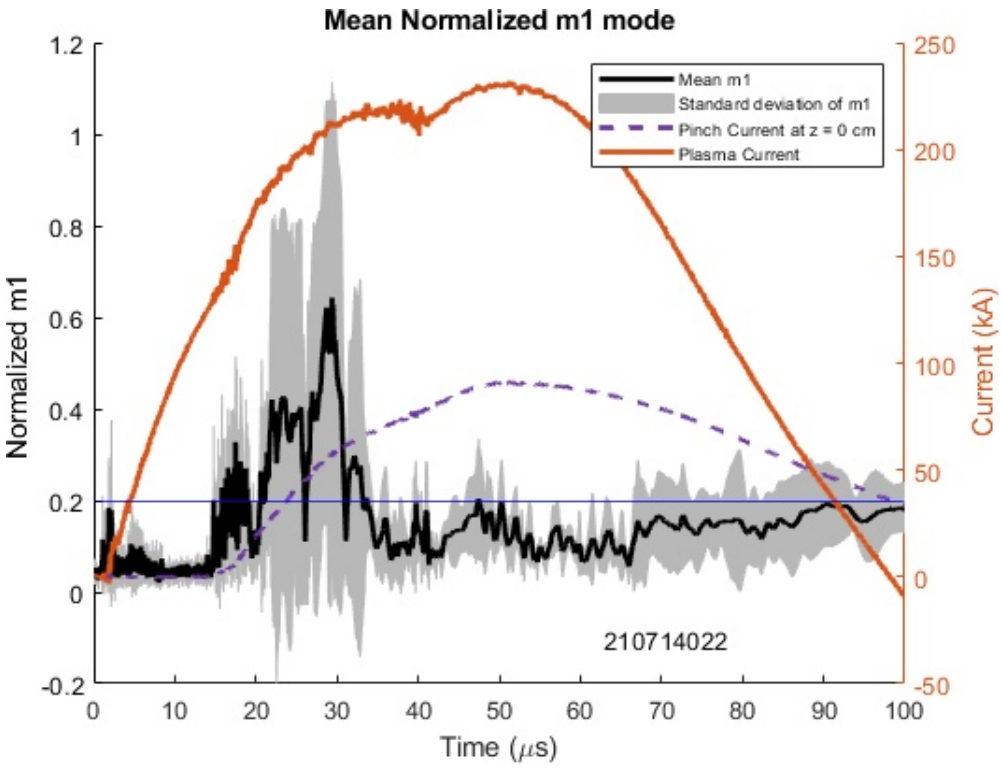

Figure 4.9: Plot of normalized m_1, plasma current and pinch current for a representative pulse at [6,8] kV. Peak pinch current occurs at 50 μs and sits within a quiescent period lasting from 48 to 90 μs. The ICCD trigger times tested were 45 and 55 μs.

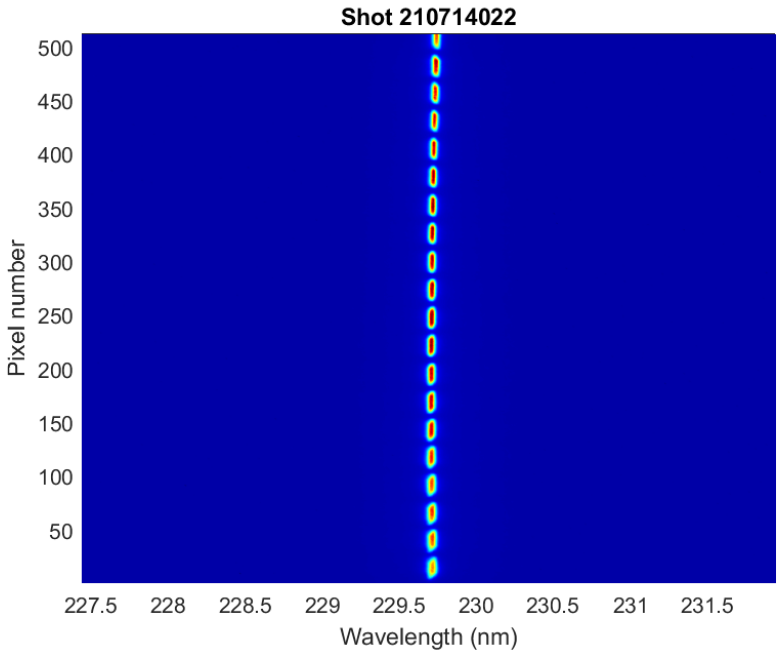

Figure 4.10: Spectrum of wide fiber bundle chords for pulse 210714022, representative of the data set for ICCD trigger variations. Chords are distinct, below saturation, and uniformly illuminated from chord 5 and above. The first 5 chords are broader and less defined.

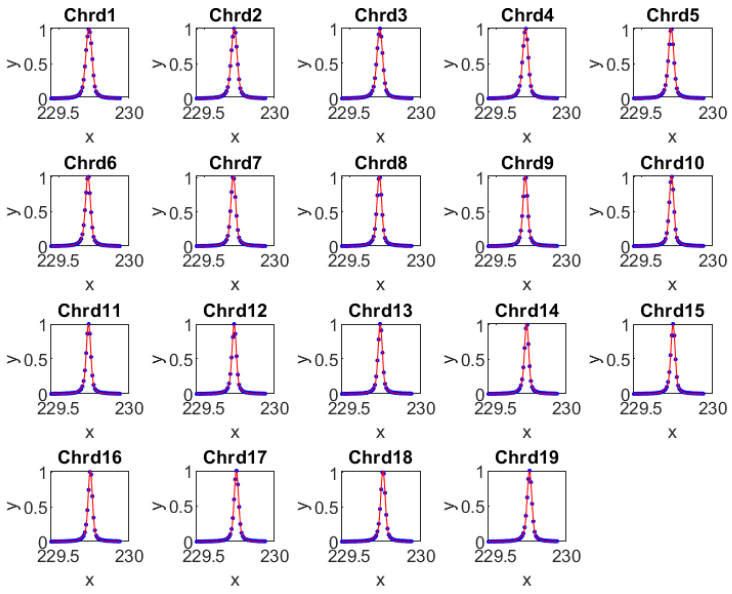

Figure 4.11: Gaussian profiles fitted to each chord for calculation of ion temperature from the C-III impurity. The first 5 chord fits are wider, corresponding to the broader spectral data in Figure 4.10. Data are for pulse 210714022.

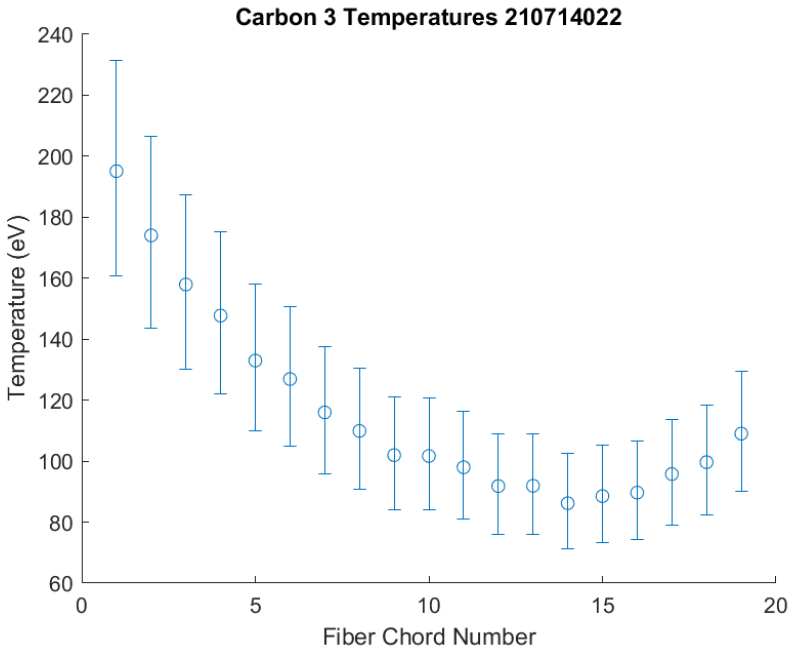

Figure 4.12: Ion temperatures from broadening of C-III impurities for each chord with confidence interval bars. Bars are larger for the low chord numbers and decrease for the central chords.

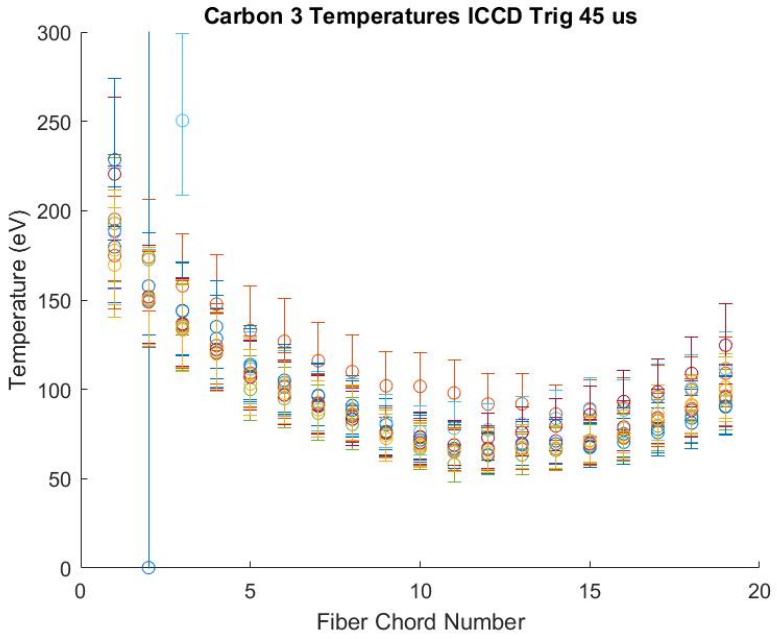

(a)

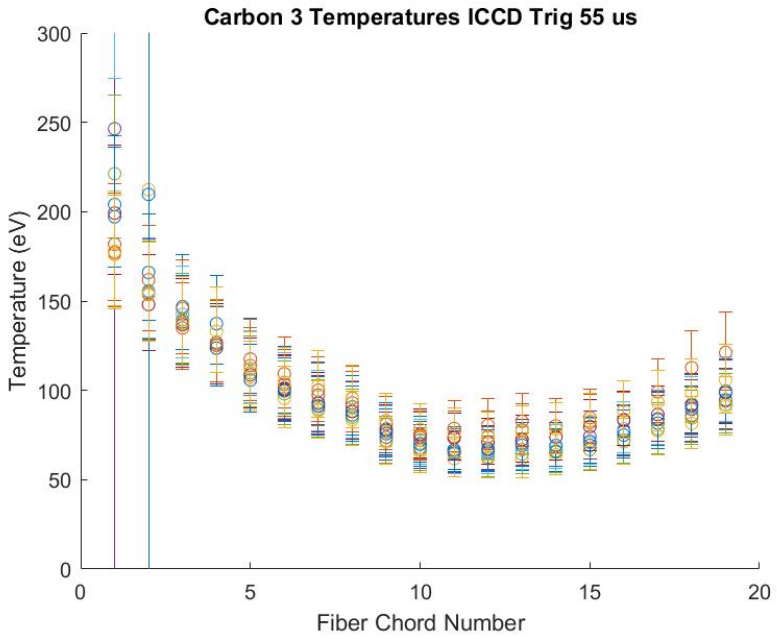

(b)

Figure 4.13: Ion temperatures measured by the C-III impurity line taken at P0. 10 pulses were taken for ICCD trigger at 45 μs (a) and 10 pulses at 55 μs (b). Measured temperatures are similar for both timings, with low spread between pulses. Data are for pulses 210714021-210714030 and 210714031-210714040 respectively.

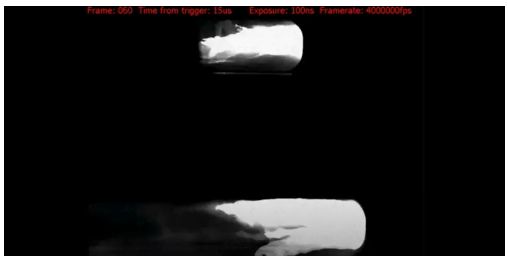

(a) 45 μs ICCD trigger for pulse 210714022

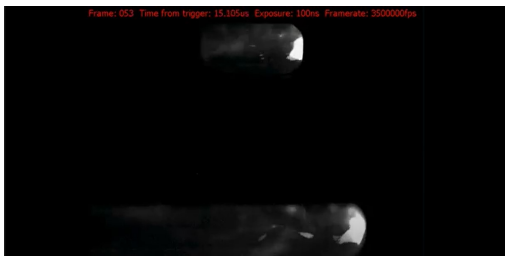

(b) 45 μs ICCD trigger for pulse 210714040

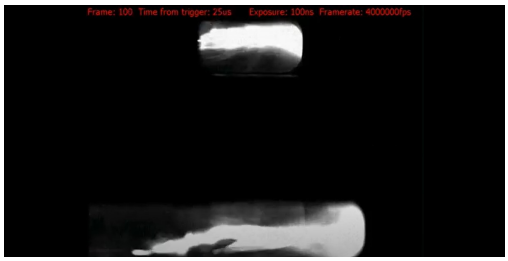

(c) 55 μs ICCD trigger for pulse 210714022

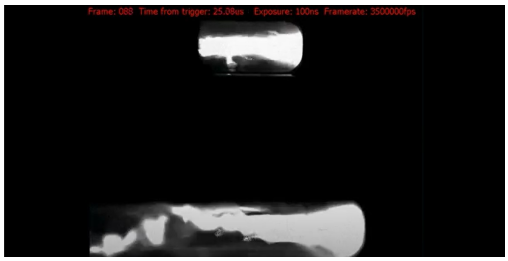

(d) 55 μs ICCD trigger for pulse 210714040

Figure 4.14: Kirana high-speed images showing variability of pinch behavior for identical settings. These images were taken with the periscope installed: the top window view is above the side window view. The curved border between the bright signal and dark background is the slot in the outer electrode. The spectroscopy telescope viewed light from P0. The downstream direction is to the left.

4.4 Variation of Axial Location

The set of pulses described in the previous section was repeated after moving the telescope to P15 in order to determine the ion temperature further downstream. Comparison of temperatures at different axial locations is useful in identifying regions of higher or lower ion energies. Because the operational parameters are identical to the pulses described in the previous section, the representative data from Figure 4.9 is referenced. Figures 4.15, 4.16, and 4.17 show the spectrum, Gaussian fits, and computed ion temperature respectively for pulse 210721023. The ICCD was triggered at 45 μs. Unlike the spectrum in Figure 4.10, the background intensity appears to be much brighter relative to the chords. This was an effect observed for a majority of the pulses in this set, and likely occurs when one or more pixels in the ICCD outputs a very large negative intensity value. Relative to this large negative value, the background appears much closer in intensity to the chords, so takes on a brighter color in the gradient scheme. This occurs when the ICCD records an overall lower level of light intensity. The brightest chord in affected spectra for measurements at P15 is usually an order of magnitude smaller than the brightest chord for P0 measurements. A similar effect is noted when collecting light for low voltage discharges between 1 - 3 kV. Images from the Kirana in Figure 4.19 show off-axis movement of the plasma further downstream from the nose cone, which could explain the reduction in light intensity recorded.

Another feature observed in the spectrum is a secondary emission line at 231.3 nm. A number of candidate ions may be responsible: W-I at 231.3012 or 231.3170, W-II at 231.366, W-III at 231.3088, or O-II at 231.3077. Additional spectra with the spectrometer grating optimized for this wavelength are needed to determine the species with greater accuracy, but the ions listed are impurities previously observed on ZaP-HD. Because this line is only observed at P15, it suggests a greater concentration of this impurity downstream of the nose cone. For this pulse, the chord-averaged ion temperature was 142.3 eV. Omitting the outlier reduces this to 123.9 eV, which is still considerably higher than the measurement at P0. The central chord ion temperature was 88.0 eV, also greater than the measurement at P0.

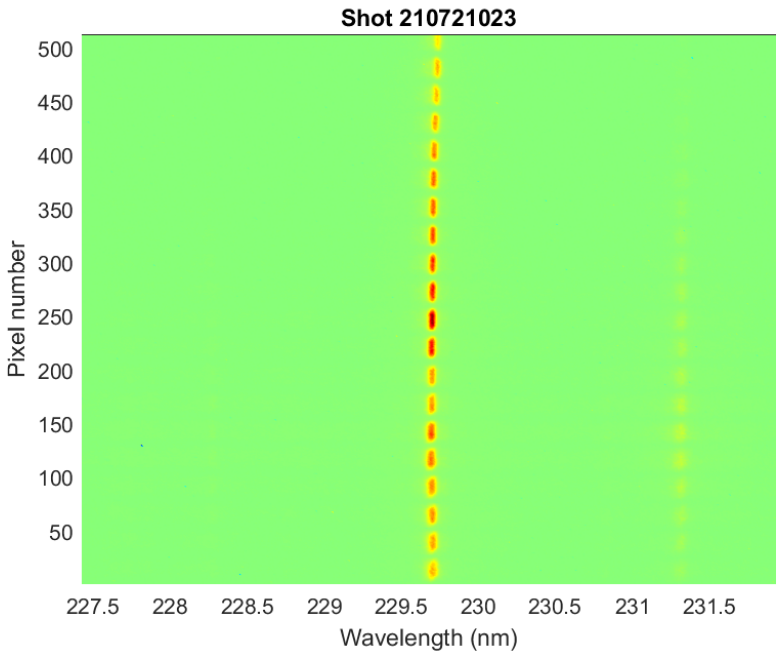

Figure 4.15: Spectrum of wide fiber bundle chords for pulse 210721023, representative of the data set for ICCD trigger variations at P15. Brightness is unevenly distributed. There is less contrast between the chords and the background, likely due to a highly negative pixel output. An additional line is visible at 231.3 nm, possibly a W or O ion impurity.

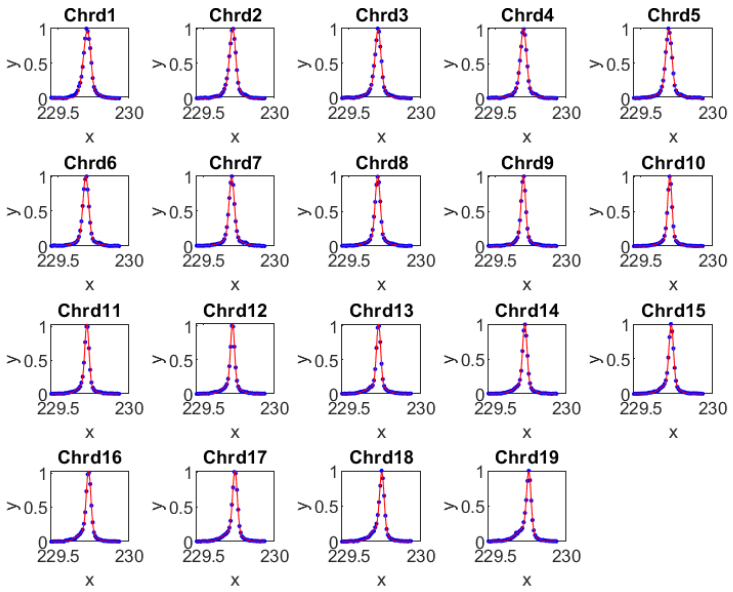

Figure 4.16: Gaussian profiles fitted to each chord for calculation of ion temperature from the C-III impurity. Chords correspond to the spectrum in Figure 4.15 for pulse 210721023.

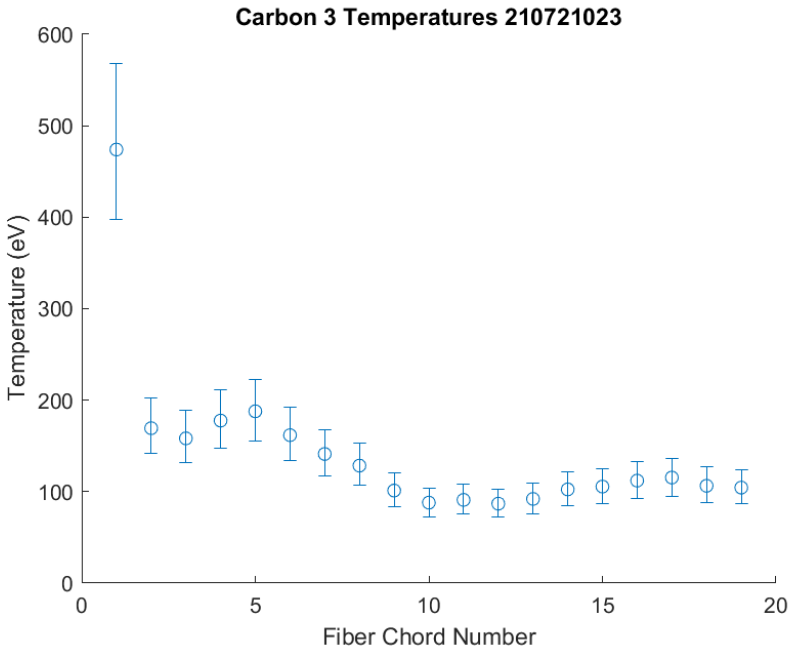

Figure 4.17: Ion temperatures for each chord with confidence interval bars. There is a large outlier for chord 1 of 474 eV, then a distribution of temperatures that decreases approaching the central chords. Chords correspond to the spectrum in Figure 4.15 for pulse 210721023.

Results from spectroscopy initially indicate a higher ion temperature at P15 if using the chord-averaged value. For a 45 μs ICCD trigger, this was 122.5 eV with 16.5 standard deviation. At 55 μs this increased to 128.8 eV and 32.5 standard deviation. However, the much larger spread indicates larger variability during the pulse. Plotting the temperatures for each data set provides a good visualization of this variability, shown in Figures 4.18a and 4.18b. Some pulses show much higher temperatures from the central chords, although a similar bowed profile is still evident. Although the confidence interval bars are large for the high temperatures at both ICCD trigger times, the lower extent remains higher than the temperatures measured at P0.

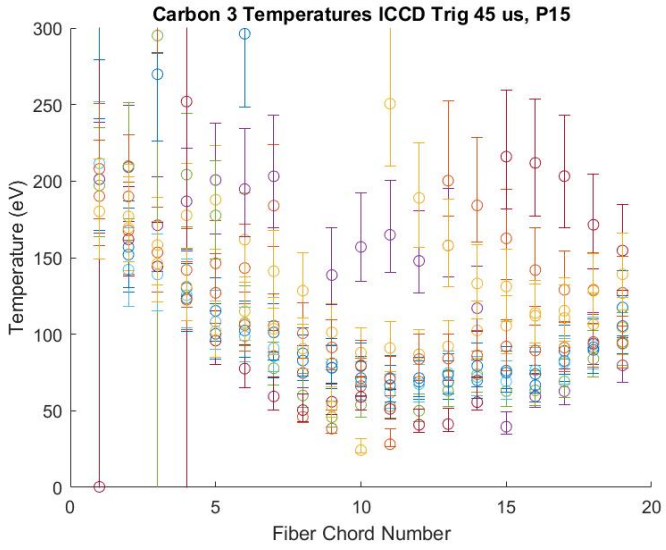

(a)

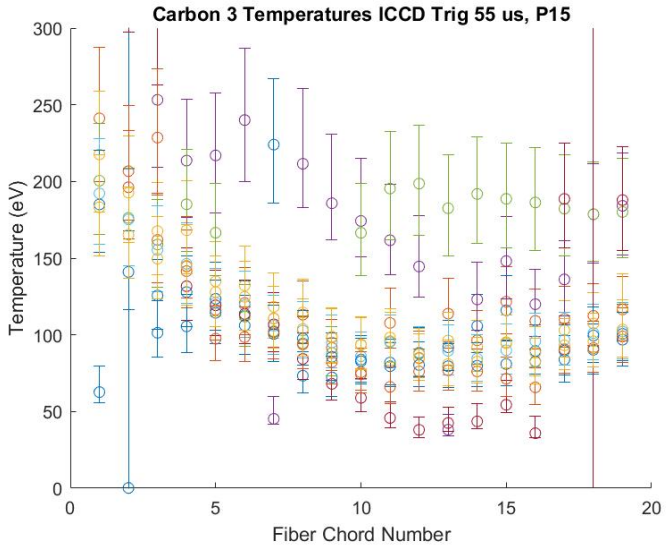

(b)

Figure 4.18: Ion temperatures measured by the C-III impurity line taken at P15. 10 pulses were taken for ICCD trigger at 45 μs (a) and 10 pulses at 55 μs (b). Measured temperatures are highly varied between pulses, possibly due to much lower light intensity recorded. Data are for pulses 210721021-210721030 and 210721031-210721040 respectively.

The Kirana images showed a similar outcome as data from P0 when comparing separate pulses at identical settings. In Figure 4.19a, the plasma is not well collimated in either view and is experiencing an instability. The bright feature in the side view splitting off from the main plasma may be an artifact of the recording. For an identical pulse in 4.19b, almost no pinch is visible in the top view while a highly offset pinch is seen in the side view. Further disparities are seen in Figures 4.19c and 4.19d. Note that the set of Kirana images shown here and previously in Figure 4.14 are pulses from two sets taken at identical settings.

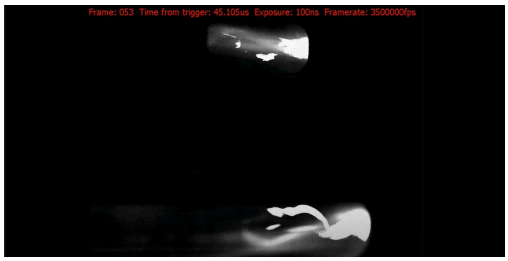

(a) 45 μs ICCD trigger for pulse 210721023

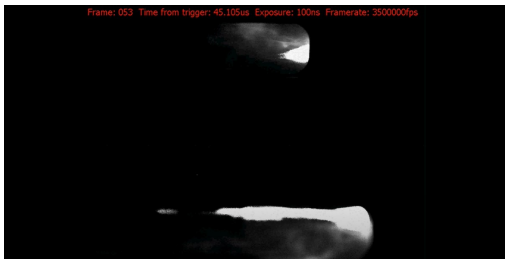

(b) 45 μs ICCD trigger for pulse 210721035

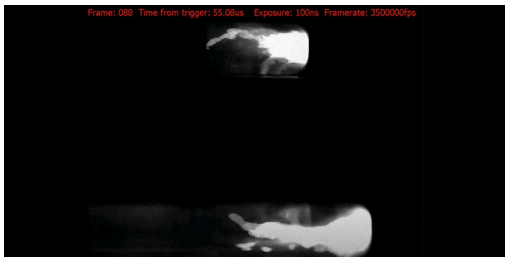

(c) 55 μs ICCD trigger for pulse 210721023

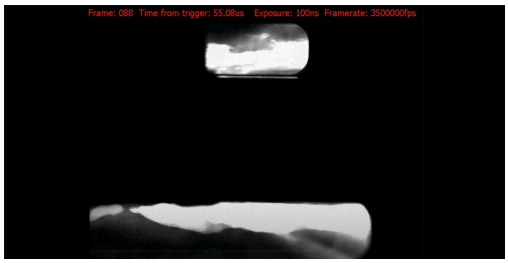

(d) 55 μs ICCD trigger for pulse 210721035

Figure 4.19: Kirana high-speed images showing variability of pinch behavior for identical settings. The spectroscopy telescope viewed light from P15. a) Pinch is clearly visible on both views, but not as defined vertically. b) Pinch is offset vertically, but not as defined in top view. c) Visible instabilities in both views. d) Defined column in both views, plasma is offset vertically.

Initial characterization of the plasma pinch produced using a graphite nose cone suggest a fairly long quiescent period up to 57 μs, defined by the normalized mean m_1. Ion temperatures measured by the Doppler broadening of the C-III ion appear to be consistent within the duration of peak pinch current, but variability seems to increase further downstream of the nose cone. However, given the limited repeatability of the plasma for identical operational parameters, inconsistencies in spectroscopy data, and a limited scope of plasma parameters measured, it is difficult to assign a strong level of confidence in these results. Despite this, a wealth of data has been produced that will inform further improvements to machine operation and diagnostic optimization for the graphite nose cone.

4.5 Identifying Additional Impurities

The line radiation of multiple additional impurities was observed at various wavelengths using the spectroscopy system. These identification pulses were taken at 3 kV compression voltage and 5 kV acceleration voltage. For the spectra shown in Figure 4.20, the oblique telescope was viewing P0, and the ICCD triggered at 50 μs with a 10 μs gate width. A split fiber configuration was installed, with two rows of ten fibers. Ten chords appear in the spectra instead of ten, possibly due to a slight misalignment of the bundle with the focal point of the telescope. Additionally, the coarse diffraction grating was used on the spectrometer for a wide range of wavelengths, at the expense of resolution. Therefore, all identifications other than well-known lines such as C-III and H-α are tentative. In Figure 4.20a, a strong C-III line appears at 229.7 nm beside a dim line at 212.4 nm, which may be B-II or Cu-I. A possible source of boron is the insulating cap of the magnetic field probes. Sputtered copper and tungsten may be present in the vacuum chamber from the previous nose cone, as shown in Figures 4.20b and 4.20c. H-α appears near its expected wavelength in Figure 4.20d. C-I may be present as well, as evidenced in Figures 4.20b and 4.20d. Figure 4.20b shows numerous lines grouped closely together, which may be evidence of various ionization states associated with copper and tungsten, which are transition metals.

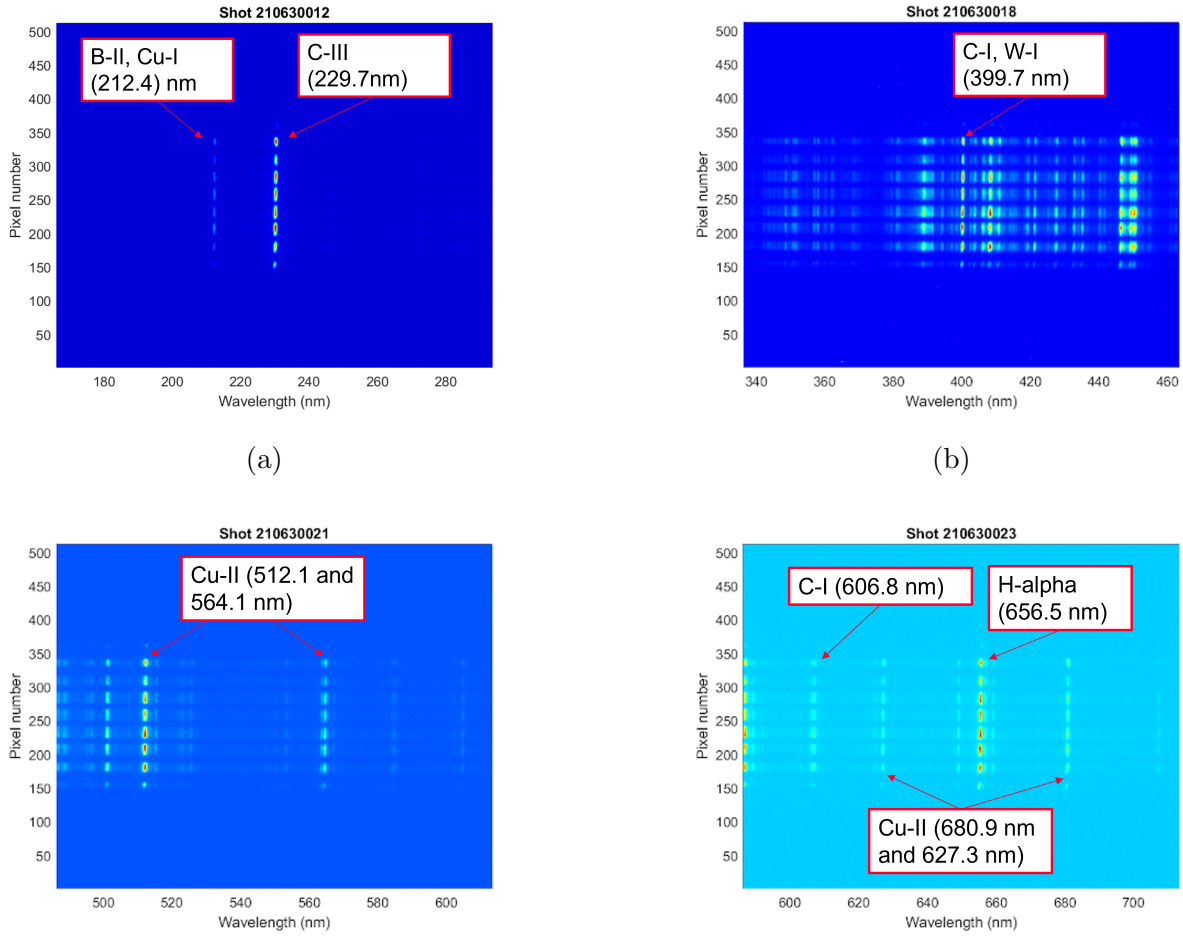

Figure 4.20: Line radiation spectra of numerous impurities in the ZaP-HD plasma with the graphite nose cone. The coarse diffraction grating on the spectrometer was used for a wide range of wavelengths, therefore species identification is tentative. Multiple ionization states of carbon and copper are evident along with boron and tungsten. A strong H-α line appears near its expected wavelength.

The presence of several bright emission lines indicate multiple impurity species that contaminate the ZaP-HD plasma. These impurities radiate energy and may be redeposited on the electrode surface. Subsequent sputtering of deposited material recycles impurities back into the plasma. Individual impurity ions experience a range of plasma conditions and ionization states, complicating analysis of PMI processes. Analysis of impurities is facilitated by assuming coronal equilibrium, where the collisional ionization and recombination processes are dynamically balanced. Using an electron temperature of 1 keV and electron density of 2×10^{17} cm^{-3} from previous ZaP-HD operation with the copper nose cone [33] suggests τ_{ss} of half a microsecond, where this is the time to reach a steady state within 1% of coronal equilibrium values. According to the carbon impurity plots from Carolan [8], at these plasma parameters, fully-ionized carbon should be present. While C-III was predominantly used in this study, C-V and higher states would provide higher ion temperature measurements. Previous measurements with the copper nose cone show a peaked C-V temperature on the pinch axis [13], which may be a useful method of characterizing the plasma core. Measurements of electron temperature and density would allow the use of the Carolan plots in determining the impurity ionization states, abundances, and power radiated.

Chapter 5

DISCUSSION OF RESULTS

It is important to place the results within the context of the main objective of plasma-material interactions study. To do this, the measured plasma parameters must be related to the relevant PMI processes discussed in Chapter 3. The ion temperature was the main plasma parameter measured in this study. The performance of the graphite must also be placed in comparison to that of the tungsten-sprayed copper. A few pulses were taken at identical parameters for this purpose. The ion temperature and pinch stability for each material are compared using the established analysis methods. While the scope of this initial investigation was necessarily limited, some preliminary conclusions may be drawn, and avenues of further exploration and improvement have presented themselves.

5.1 Relating Plasma Parameters to PMI Processes

The measured ion temperature from C-III impurity emission can be used to calculate the sound speed from Equation 3.6. Because of the significant variation observed for pulses taken at P15, the twenty pulses with the spectroscopy telescope located at P0 are used to deliver a more precise calculation. Currents and mode data appear in Figure 4.9, spectroscopy in Figures 4.11 and 4.12, Kirana images in 4.14a and 4.14c, and temperatures in Figure 4.13 from Section 4.3. The assumptions of $T_i = T_e$, and $\gamma = 1$ isothermal flow apply. Figure 5.1 shows the campaign-averaged sound speeds for C-III for each fiber chord. The error bars represent standard deviation for twenty pulses from 210714021 - 210714040.

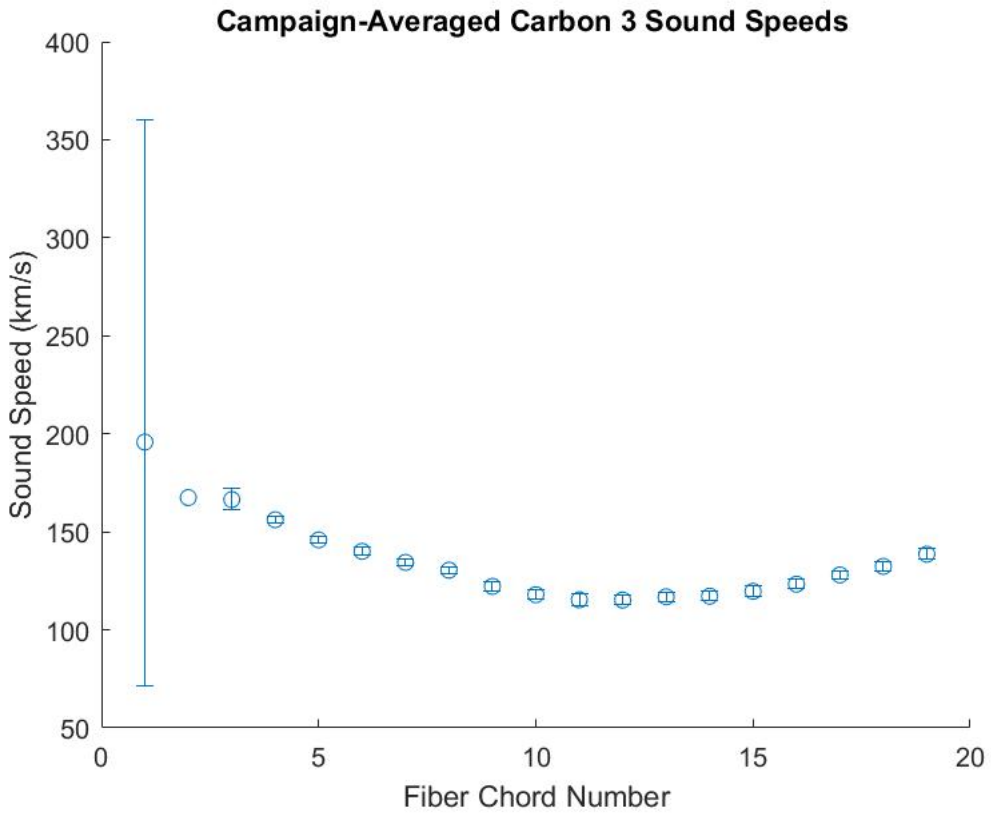

Figure 5.1: Campaign-averaged sound speeds for each chord of the wide fiber based on ion temperatures from C-III Doppler broadening. Error bars represent the standard deviation for twenty pulses. The pulses in this data used 6 kV compression bank voltage and 8 kV acceleration bank voltage. Pulses are 210714021 - 210714040.

The average sound speed across all fibers is 136.0 km/s, while the central chord value is 117.9 km/s. As noted previously, the edge chord measurement varies significantly between pulses. Despite this, variation in sound speed is fairly consistent for the remainder of the chords. The sound speeds from this set of pulses are comparable to the values calculated by Forbes [13] for a plasma with 3 kV compression bank voltage, C-III ion temperatures, and the copper nose cone installed. A much larger charge voltage is required for the recent pulses to achieve a similar sound speed. However, the strength of this comparison is limited due to varied operational parameters such as the gas mix, line pressure, and spectroscopy configuration. Previous operation used a mixture of methane and hydrogen, with methane concentration varying from 5 and 50%. The line pressure to the inner valve for this data set was also lower than the pulses with the copper nose cone.

5.2 Comparison of Plasma Parameters and Stability for Copper and Graphite

A direct comparison between the copper and the graphite nose cones was performed by replicating the operational parameters. Table 5.1 summarizes the exact operational parameters.

Copper Pulse Number	**Graphite Pulse Number**	V_C **(kV)**	V_A **(kV)**	**Compression Delay** (μ**s)**	P_{gas} **I/O (torr)**	**ICCD Trigger** (μ**s)**
210127006	210721085 210721086 210721087	3	5	20	4300/3300	20
210127007	210721088 210721089 210721090	5	7	20	4300/3300	35
210224014	210721075 210721076 210721077	5	7	20	4300/3300	50

Table 5.1: Operational parameters for replication of copper pulses.

Recent spectroscopy data with the copper nose cone are limited, and some settings such as the gain and gate time were not fully documented. While there are substantial run campaigns

available to replicate over the last few years, due to time constraints these were unable to be fully explored. Some other differences include the use of a gas mix for the copper pulses. A 5-50% mix by pressure of methane and hydrogen was used to seed the plasma with a carbon impurity that is unnecessary with a graphite nose cone installed. Furthermore, the copper data was taken with the perpendicular telescope viewing P15, while the graphite data uses the oblique telescope viewing P0. The pulses with the copper nose cone were selected for spectroscopy results for having minimal outliers and spectral aberrations. The condition of the copper nose cone for these pulses was similar to that shown in Figure 3.2.

The comparisons encompass two voltage settings, with compression voltage at 3 and 5 kV. Compression delay times were identical, and the ICCD trigger time was varied. Three pulses were taken at each setting for the graphite nose cone. The following plots compare the measured ion temperature from C-III Doppler broadening across the fiber chords for two of the replicated copper pulses. Figure 5.2a compares pulses for 3 kV compression bank voltage. A similar profile across the chords is evident, with higher temperatures recorded by one side of the bundle. In general, the copper nose cone produced higher ion temperatures, although the values begin to overlap at the central chords. Figure 5.2b shows a more distinct difference in ion temperatures, although the first three chords returned excessively high temperatures.

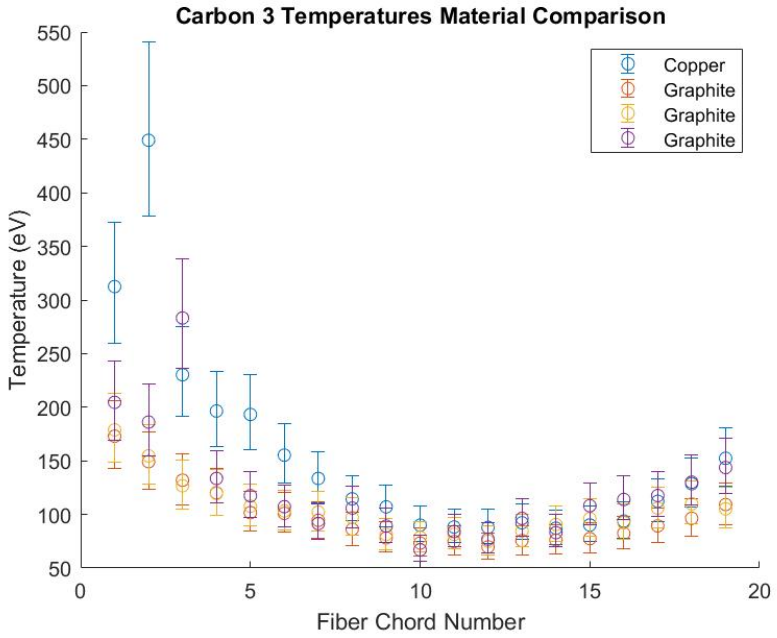

(a) 3 kV compression bank voltage

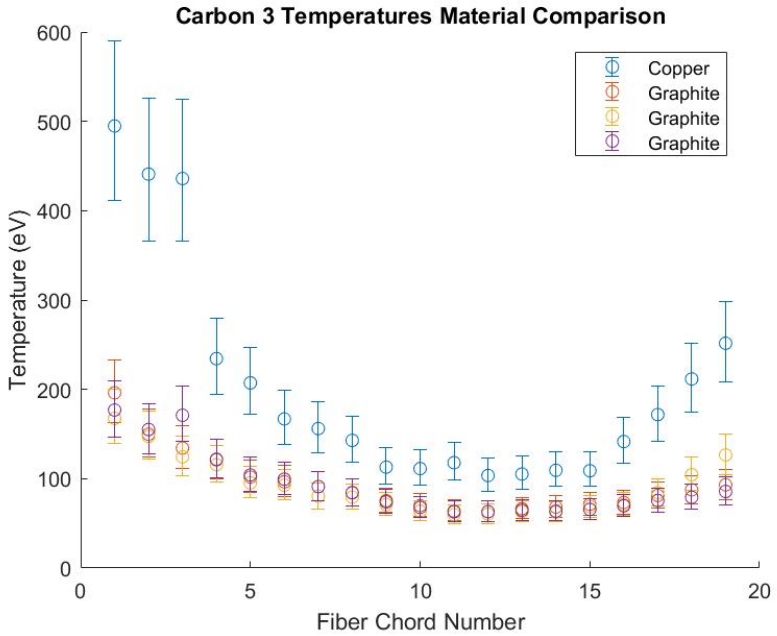

(b) 5 kV compression bank voltage

Figure 5.2: Comparison of ion temperatures measured from C-III Doppler broadening for copper and graphite nose cones. Three pulses with graphite were taken with identical operational parameters as the reference copper pulse. In general, the measured ion temperatures for copper are higher than for graphite. The reference copper nose cone pulse was 210127006 for 3 kV compression voltage, and 210127007 for 5 kV compression voltage.

One possible reason for the lower ion temperatures for the graphite nose cone is increased sputtering. Because carbon is a low-Z element, the threshold energy for physical sputtering is lower than copper, and significantly lower for the tungsten layer. As calculated in Section 3.1.2, the tungsten threshold energy for physical sputtering is more than ten times greater than for carbon. Because of the cooling effect of radiating impurities, an increased level could lower the overall temperature. Although a high-Z impurity such as tungsten would radiate more energy, there may be other effects that cause the lower temperature with carbon impurities. Chemical sputtering may be a more dominant phenomenon with the graphite nose cone, contributing to the impurity species and concentration. Making the rough assumption that the ion temperature corresponds to the energy of impact, and that surface temperature is sufficiently high, then the measured values meet the conditions specified in Section 3.1.2 for maximum methane impurity concentration. The higher ion temperatures for a copper nose cone are reflected in the chord-averaged value. The average ion temperature at 3 kV compression voltage is 137 and 109 eV for copper and graphite respectively, and 153 and 93 eV respectively for 5 kV compression voltage. Interestingly, the ion temperature decreased at the higher compression voltage setting for the graphite.

5.3 Suggested Improvements

Several improvements can be made in terms of machine operation and diagnostic capability. Significant variability was noted throughout the run campaigns, increasing the standard deviations of the quantities presented. A greater number of pulses would naturally help in this respect, but should be accompanied by mitigation of the sources of variability. These include the amount of neutral gas injection, the distribution of the gas in the annular region between the middle and inner electrodes, and voltage transients associated with capacitor bank discharge. In other words, the energy and fuel input control must be improved.

The addition of time-resolved ion Doppler spectroscopy would vastly improve the ability to reference the temperature with existing time-resolved diagnostics, since the existing method only provides an instantaneous measurement. A procedure for this has already

been established and is a logical next step for this diagnostic. Furthermore, density measurements through laser interferometry would enable computation of particle flux density, a useful parameter in many PMI processes. Three-Dimensional Digital Holographic Interferometry (DHI) in particular can reconstruct electron density structures along the pinch. This provides quantifiable information on the pinch radius and movement away from the central axis. Finally, the Kirana high-speed camera is currently limited to the spectrum of visible wavelengths. This typically comes from line radiation of hydrogen in cooler regions of the plasma and bremsstrahlung radiation in the hotter regions. Recording ultraviolet emission may enhance imaging of the hot plasma core, and can be achieved by installing a phosphor intensifier unit. In addition, a method to accurately extract lengths and locate the plasma from Kirana images would be useful to compare with other diagnostics.

While further replication is needed for a direct comparison between materials, focus should eventually turn to increasing the plasma parameters for the graphite. Due to the bulk of pulses described in this study operating at 6 kV compression and 8 kV acceleration voltage, there is still room to operate at the maximum charge voltage of 9 kV. The lower voltage was selected to minimize large voltage transients that may damage the device. Furthermore, other operational parameters such as the gas injection and various timings should be optimized to increase pinch performance. If chemical sputtering is indeed limiting the maximum ion temperature measured, a method for quantifying this during operation should be developed. In addition, finding suitable diagnostic settings to most accurately capture information from the plasma is an intensive process, and may require specific adjustments as the discharge voltage and plasma current increase.

Chapter 6

CONCLUSION

The ZaP-HD device played an essential role in developing the concept of the sheared-flow-stabilized Z pinch by demonstrating reduced instability modes for greater plasma parameters than the original ZaP device. This capability also makes it a unique platform for the study of plasma-material interactions in a high energy density environment. Furthermore, PMI research for a tangential magnetic field is an area with much left to study. The characterization performed involved scans of the capacitor bank charge voltage, compression bank time delay, and axial location and collection time of spectroscopy. The power supplies were successfully discharged up to 7 kV compression and 9 kV acceleration voltage, noting the expected increase in pinch current and a slight increase in ion temperature measured from Doppler broadening of the C-III impurity ion. However, the bulk of pulses taken during this campaign were at a lower voltage setting to minimize potential damage to the device. Delaying the compression bank discharge ensures enough plasma has arrived in the assembly region to form a pinch, and different delays may be required for different voltage settings. Quiescent periods appeared to peak for a 24 μs delay and fixed voltage. The trigger for the ICCD, which collects light for ion Doppler spectroscopy, was tested at 45 and 55 μs, marking regions just before and after the peak current. Ion temperatures showed few differences between the two times. Studying line radiation further downstream of the pinch revealed highly inconsistent ion temperatures, perhaps due to instabilities in the plasma resulting in reduced light intensity recorded. Overall, the graphite electrode produced quiescent periods up to 57 μs, and ion temperatures up to 100 eV for pinch currents up to 100 kA. While the ion temperatures appear to be lower than those measured using the copper nose cone, stability and current values are similar between the two materials. Enhanced physical and

chemical sputtering may be responsible for this finding. Evidence for a variety of impurities in addition to carbon was observed, including boron, tungsten, and copper. Plasma parameters indicate that C-V should be present in the plasma, which may be used for higher ion temperature measurements in the plasma core. Further experimentation is needed to verify these results, a process which includes enhancement of the diagnostic suite and mitigation of pulse variability.

The experimental efforts described in this thesis make up a preliminary exploration into the characterization of graphite as an electrode material, and a key component of the larger investigation into PMI on the ZaP-HD device. While the PMI study encompasses both the effect of the material on the pinch and the material response, this thesis focused mainly on pinch characterization. The graphite nose cone will form the base component of a design with a removable insert, allowing faster removal of samples and better control of total plasma exposure. Simultaneously, a variety of alternative electrode materials can be tested by machining an insert, or coating an insert on the graphite substrate. A variety of tungsten and copper alloys, metal foams, and metal coatings are potential test materials. Selecting the duration and intensity of exposure is made easier with the new design. Inserts will undergo ex-situ surface topography analysis before and after plasma exposure. SEMs provide rapid, high resolution images of surface features and equipped EDS handles elemental identification. Depth measurements will be done with an optical profilometer and atomic force microscope, depending on the target surface area and resolution required. These methods will first be performed on the existing graphite nose cone, from which a sample will be removed.

Future work involves expanding the diagnostic suite. DHI, time-resolved spectroscopy, and enhanced Kirana measurements will provide additional plasma parameter measurements. Calculation of the bulk flow velocity should also be performed to compare the radial shear flow to the threshold required for stability. A band pass filter for the Kirana can be installed to view bremsstrahlung radiation. This filters hydrogen line radiation that typically occurs in cooler regions of the plasma, leaving behind the bremsstrahlung from hotter regions. Bremsstrahlung radiation may also be measured using spectroscopy. An estimate of Z_{eff}

can then be obtained with separate measurements of electron temperature and density, a useful measure of impurity contamination. A method for in-situ measurements of sputtering yield or concentration should be developed. For example, impurity concentrations were calculated by measuring local flux density using visible spectroscopy on JET [3] for metal, carbon, and oxygen impurities. This could provide a measurement of carbon sputtered from the graphite nose cone during operation. It may be useful to combine this method with the seeding of a known quantity of impurity, perhaps a noble gas if a consistently strong emission line can be determined. Another possibility is operating the device with helium instead of hydrogen, which could be a method for distinguishing between physical and chemical sputtering. Measurements of surface temperature using IR pyrometry would be useful as an additional in-situ, non-perturbing diagnostic, but must bypass the IR-absorbing fused silica windows currently installed. This would be exceptionally useful in studying the conditions for chemical sputtering, which relies heavily on the surface temperature.

While sheared flows have proven effective at mitigating instabilities, it remains to be seen if they will continue to do so as pinch current and plasma parameters increase. In order to achieve and sustain higher fusion performance, these are necessary increases based on the latest understanding. As a result, it is crucial to monitor the material behavior so effects such as chemical sputtering do not release substantial amounts of impurities into the plasma. Doing so increases radiation losses, requiring a greater power input into the device, and lowering overall reactor efficiency. If other methods of stabilization are needed at higher plasma parameters, the dominant PMI processes may change. Fusion-capable devices like FuZE introduce a neutron flux [36] to the electrode materials along with increased energy density, bringing neutron activation and safety considerations into the fold. Furthermore, a reactor design may include flowing liquid metal electrodes [12], for which diagnostic methods must be developed. Simulation of plasma-material interactions would be a powerful tool to inform experimental studies. These considerations will form an essential part of the effort to establish the Z pinch as a solution to the challenge of fusion.

BIBLIOGRAPHY

[1] J. Abrahamson. Graphite sublimation temperatures, carbon arcs and crystallite erosion. *Carbon*, 12(2):111–141, 1974.

[2] Vivek Bakshi, Ahmed Hassanein, Jean-Paul Allain, Tatiana Burtseva, Zeke Insepov, J Brooks, Isak Konkashbaev, V Moroszov, Valeryi Sizyuk, Vladimir Tolkach, and et al. *Electrode and Condenser Materials for Plasma Pinch Sources*, volume PM149, page 916–953. SPIE Press, 2006.

[3] K.H. Behringer. Spectroscopic studies of plasma-wall interaction and impurity behaviour in tokamaks. *Journal of Nuclear Materials*, 145-147:145–153, 1987.

[4] Willard H. Bennett. Magnetically self-focussing streams. *Phys. Rev.*, 45:890–897, Jun 1934.

[5] David Bohm, Andrew Guthrie, and Raymond Kornelious Wakerling. *Minimum Ionic Kinetic Energy for a Stable Sheath*, page 77. McGraw-Hill, 1949.

[6] Joan Lisa. Bromberg. *Fusion: science, politics, and the invention of a new energy source*. MIT Press, 1985.

[7] V.P. Budaev, Yu.V. Martynenko, S.A. Grashin, R.N. Giniyatulin, I.I. Arkhipov, A.V. Karpov, P.V. Savrukhin, E.A. Shestakov, R.Yu. Solomatin, L.B. Begrambekov, N.E. Belova, S.D. Fedorovich, L.N. Khimchenko, and V.M. Safronov. Tungsten melting and erosion under plasma heat load in tokamak discharges with disruptions. *Nuclear Materials and Energy*, 12:418–422, 2017. Proceedings of the 22nd International Conference on Plasma Surface Interactions 2016, 22nd PSI.

[8] P. G. Carolan and V. A. Piotrowicz. The behaviour of impurities out of coronal equilibrium. *Plasma Physics*, 25(10):1065–1086, oct 1983.

[9] E. L. Claveau, U. Shumlak, B. A. Nelson, E. G. Forbes, A. D. Stepanov, T. R. Weber, Y. Zhang, and H. S. McLean. Plasma exhaust in a sheared-flow-stabilized z pinch. *Physics of Plasmas*, 27(9):092510, 2020.

[10] Daniel J. Den Hartog. How to set up and use the iccd viewing telescopes on zap, Jan 2003.

[11] E. G. Forbes and U. Shumlak. Spatio-temporal ion temperature and velocity measurements in a z pinch using fast-framing spectroscopy. *Review of Scientific Instruments*, 91(8):083104, 2020.

[12] Eleanor G. Forbes, Uri Shumlak, Harry S. McLean, Brian A. Nelson, Elliot L. Claveau, Raymond P. Golingo, Drew P. Higginson, James M. Mitrani, Anton D. Stepanov, Kurt K. Tummel, Tobin R. Weber, and Yue Zhang. Progress toward a compact fusion reactor using the sheared-flow-stabilized z-pinch. *Fusion Science and Technology*, 75(7):599–607, 2019.

[13] Eleanor Glynis Forbes. *Diagnostic development and plasma-material interaction studies on the ZaP-HD device*. University of Washington, Seattle, 2020.

[14] Jeffrey P. Freidberg. *Plasma physics and fusion energy*. Cambridge University Press, 2007.

[15] Raymond Peter Golingo. *Formation of a Sheared Flow Z-Pinch*. University of Washington, Seattle, 2003.

[16] M. R. Gomez, S. A. Slutz, A. B. Sefkow, D. B. Sinars, K. D. Hahn, S. B. Hansen, E. C. Harding, P. F. Knapp, P. F. Schmit, C. A. Jennings, T. J. Awe, M. Geissel, D. C. Rovang, G. A. Chandler, G. W. Cooper, M. E. Cuneo, A. J. Harvey-Thompson, M. C. Herrmann, M. H. Hess, O. Johns, D. C. Lamppa, M. R. Martin, R. D. McBride, K. J. Peterson, J. L. Porter, G. K. Robertson, G. A. Rochau, C. L. Ruiz, M. E. Savage, I. C. Smith, W. A. Stygar, and R. A. Vesey. Experimental demonstration of fusion-relevant conditions in magnetized liner inertial fusion. *Phys. Rev. Lett.*, 113:155003, Oct 2014.

[17] M. G. Haines. Fifty years of controlled fusion research. *Plasma Physics and Controlled Fusion*, 38(5):643–656, may 1996.

[18] M. G. Haines, S. V. Lebedev, J. P. Chittenden, F. N. Beg, S. N. Bland, and A. E. Dangor. The past, present, and future of z pinches. *Physics of Plasmas*, 7(5):1672–1680, 2000.

[19] I. H. Hutchinson. Principles of plasma diagnostics: Second edition. *Plasma Physics and Controlled Fusion*, 44(12):2603–2603, nov 2002.

[20] B. B. Kadomtsev. Hydromagnetic Stability of a Plasma. *Reviews of Plasma Physics*, 2:153, January 1966.

[21] A. Kirschner. Erosion and deposition mechanisms in fusion plasmas. *Fusion Science and Technology*, 53(2T):259–277, 2008.

[22] A. Kramida, Yu. Ralchenko, J. Reader, and and NIST ASD Team. NIST Atomic Spectra Database (ver. 5.8), [Online]. Available: `https://physics.nist.gov/asd` [2021, July 27]. National Institute of Standards and Technology, Gaithersburg, MD., 2020.

[23] I.V. Kurchatov. On the possibility of producing thermonuclear reactions in a gas discharge. *Journal of Nuclear Energy (1954)*, 4(2):193–202, 1957.

[24] Jürgen Küppers. The hydrogen surface chemistry of carbon as a plasma facing material. *Surface Science Reports*, 22(7):249–321, 1995.

[25] Ch. Linsmeier, M. Rieth, J. Aktaa, T. Chikada, A. Hoffmann, J. Hoffmann, A. Houben, H. Kurishita, X. Jin, M. Li, A. Litnovsky, S. Matsuo, A. von Müller, V. Nikolic, T. Palacios, R. Pippan, D. Qu, J. Reiser, J. Riesch, T. Shikama, R. Stieglitz, T. Weber, S. Wurster, J.-H. You, and Z. Zhou. Development of advanced high heat flux and plasma-facing materials. *Nuclear Fusion*, 57(9):092007, jun 2017.

[26] B.V. Mech, A.A. Haasz, and J.W. Davis. Isotopic effects in hydrocarbon formation due to low-energy h+/d+ impact on graphite. *Journal of Nuclear Materials*, 255(2):153–164, 1998.

[27] Angelica Ottaviano, Anirudh Thuppul, John Hayes, Chris Dodson, Gary Z. Li, Zhitong Chen, and Richard E. Wirz. In situ microscopy for plasma erosion of complex surfaces. *Review of Scientific Instruments*, 92(7):073701, 2021.

[28] K. U. Riemann. The bohm criterion and sheath formation. *Journal of Physics D: Applied Physics*, 24(4):493–518, apr 1991.

[29] D.L. Rudakov, T. Abrams, R. Ding, H.Y. Guo, P.C. Stangeby, W.R. Wampler, J.A. Boedo, A. Briesemeister, J.N. Brooks, D.A. Buchenauer, I. Bykov, C. Chrobak, R.P. Doerner, D. Donovan, J.D. Elder, M.E. Fenstermacher, J. Guterl, E. Hinson, E.M. Hollmann, C.J. Lasnier, A.W. Leonard, A.G. McLean, R.A. Moyer, R.E. Nygren, D.M. Thomas, E.A. Unterberg, J.G. Watkins, and C.P.C. Wong. DiMES PMI research at DIII-D in support of ITER and beyond. *Fusion Engineering and Design*, 124:196–201, 2017. Proceedings of the 29th Symposium on Fusion Technology (SOFT-29) Prague, Czech Republic, September 5-9, 2016.

[30] V. D. Shafranov. The stability of a cylindrical gaseous conductor in a magnetic field. *The Soviet Journal of Atomic Energy*, 1(5):709–713, Oct 1956.

[31] U. Shumlak. Z-pinch fusion. *Journal of Applied Physics*, 127(20):200901, 2020.

[32] U. Shumlak and C. W. Hartman. Sheared flow stabilization of the $m = 1$ kink mode in Z pinches. *Phys. Rev. Lett.*, 75:3285–3288, Oct 1995.

[33] U. Shumlak, B. A. Nelson, E. L. Claveau, E. G. Forbes, R. P. Golingo, M. C. Hughes, R. J. Oberto, M. P. Ross, and T. R. Weber. Increasing plasma parameters using sheared flow stabilization of a z-pinch. *Physics of Plasmas*, 24(5):055702, 2017.

[34] P. C. Stangeby. *The plasma boundary of magnetic fusion devices*. Institute of Physics Pub., 2000.

[35] George Thomson. Thermonuclear fusion: The task and the triumph. *New Scientist*, 3(63):10–12, Jan 1958.

[36] Y. Zhang, U. Shumlak, B. A. Nelson, R. P. Golingo, T. R. Weber, A. D. Stepanov, E. L. Claveau, E. G. Forbes, Z. T. Draper, J. M. Mitrani, H. S. McLean, K. K. Tummel, D. P. Higginson, and C. M. Cooper. Sustained neutron production from a sheared-flow stabilized z pinch. *Phys. Rev. Lett.*, 122:135001, Apr 2019.